nature communications

Article

https://doi.org/10.1038/s41467-025-63415-0

Modulating tumor collagen fiber alignment for enhanced lung cancer immunotherapy via inhaled RNA

Received: 7 January 2025

Accepted: 19 August 2025

Published online: 30 August 2025

Check for updates

Bin Hu[1,2], William Stewart[3], Qijing Chen[1,2], Chenshuang Zhang[1,2], Zhixiang Liu[3], Xiaoyang Xu[3,4] ✉ & Xue-Qing Zhang[1,2] ✉

The clinical effectiveness of immunotherapies for lung cancers has been greatly hindered by the immune-excluded and immunosuppressive tumor microenvironment (TME) and limited pulmonary accessibility of therapeutics. Here, we develop an inhalable lipid nanoparticle (LNP) system that enables simultaneous delivery of mRNA encoding anti-discoidin domain receptor 1 (DDR1) single-chain variable fragments (mscFv) and siRNA targeting PD-L1 (siPD-L1) into pulmonary cancer cells. The secreted anti-DDR1 scFv blocks the binding of DDR1 extracellular domain to collagen, disrupting collagen fiber alignment and reducing tumor stiffness, thereby facilitating T cell infiltration. Meanwhile, PD-L1 silencing alleviates immunosuppression and preserves T cell cytotoxicity. In vivo results demonstrate that mscFv@LNP induces collagen fiber rearrangement and diminishes tumor stiffness. In both orthotopic and metastatic mouse models of lung cancer, inhalation of mscFv/siPD-L1@LNP promotes tumor regression and extends overall survival. This strategy could be broadly applicable to solid tumors and benefit other cancer immunotherapies by addressing the universally hostile TME involved in tumor progression.

Although immunotherapy is rapidly transforming cancer management[1–3], clinical outcomes are often undermined by the hostile tumor microenvironment (TME), which is molded and conditioned by cancer cells to support tumor progression[4]. The TME presents both physical and immune barriers that limit effective antitumor immunity[5]. The extracellular matrix (ECM) barrier, which constitutes TME, shapes tumor architecture and excludes tumor-infiltrating T cells[6,7]. In particular, dense and aligned collagen fibers within the ECM confine T cells and prevent their interaction with tumor cells[8]. As a key regulator of collagen fiber state, discoidin domain receptor 1 (DDR1) is overexpressed in various solid tumors and promotes tumor progression by driving immune exclusion[9]. DDR1 is activated upon binding with collagen, which simultaneously causes the shedding of the DDR1 extracellular domain (ECD) by metalloproteases to promote the alignment of collagen fibers[10–12]. Therefore, blocking the binding of DDR1 ECD to collagen is a promising strategy to alleviate immune exclusion and induce immune infiltration by disrupting the densely packed, parallelly arranged collagen fiber barrier. On the other hand, even if immune effector cells succeed in overcoming immune exclusion and reaching the vicinity of cancer cells, their function and proliferation are often compromised by immune evasion mechanisms and the resulting highly immunosuppressive TME[13,14]. Immune checkpoint blockade (ICB) therapy reactivates suppressed T cells and fosters strong immune responses against tumors, which has made significant strides in the clinical treatment of various cancers[15,16]. By blocking the PD-1/PD-L1 signaling pathway, the immunosuppressive TME could be

[1]Shanghai Frontiers Science Center of Drug Target Identification and Delivery, School of Pharmaceutical Sciences, Shanghai Jiao Tong University, Shanghai, China. [2]National Key Laboratory of Innovative Immunotherapy, Shanghai Jiao Tong University, Shanghai, China. [3]Department of Chemical and Materials Engineering, New Jersey Institute of Technology, Newark, NJ, USA. [4]Department of Biomedical Engineering, New Jersey Institute of Technology, Newark, NJ, USA. ✉e-mail: xiaoyang.xu@njit.edu; xueqingzhang@sjtu.edu.cn

effectively mitigated[17]. Therefore, reconstructing the TME through a combined strategy of collagen barrier disruption and PD-1/PD-L1 blockade, which addresses the common challenges of immune exclusion and immunosuppression encountered in solid tumor treatment, could pave the way for robust antitumor responses.

Here, we propose an inhalable lipid nanoparticle (LNP)-mediated RNA therapeutic approach that combines messenger RNA (mRNA)-mediated antibody therapy with RNA interference (RNAi)-based ICB therapy to reconstruct the TME for treating lung cancer. Achieving sufficient pulmonary accessibility and maintaining effective drug concentrations in the lungs have been major challenges for pulmonary delivery. Systemic administration typically results in broad drug distribution to non-target organs, with limited amounts reaching the lungs, thereby increasing safety risks such as cytokine release syndrome and infections[18–20]. In contrast, inhalation provides a direct route to deliver therapeutics to the lungs, achieving better local accumulation and comparable or superior therapeutic effects at significantly lower doses than systemic administration[21–24]. Inhalation allows for the in situ function of nucleic acid drugs, including gene expression and silencing, making it a safe and efficient approach for treating various lung diseases[25–27]. Leveraging our previously developed inhaled LNP platform[28], we deliver mRNA encoding anti-DDR1 single-chain variable fragments (mscFv) to act as a collagen barrier breaker within the lung cancer TME, alongside small interfering RNA targeting PD-L1 (siPD-L1) to counteract immune evasion by cancer cells and the associated immunosuppression. A single inhalation would enable the simultaneous delivery of both agents directly to the lungs, reaching lung cancer cells and reconfiguring the TME by overcoming both physical and immune barriers.

We hypothesize that upon inhalation, mscFv will be translated into anti-DDR1 scFv, which neutralizes DDR1 ECD and disrupts collagen fiber alignment to bolster immune infiltration in lung tumor-bearing mouse models. Meanwhile, siPD-L1 effectively knocks down PD-L1 expression, reversing immune evasion and the immunosuppressive TME. This strategy dismantles tumor's resistance machinery of both immune exclusion and immunosuppression, synergistically reinvigorating antitumor immunity for lung cancers (Fig. 1). Our in vivo data show that inhalation of mscFv@LNP alters the collagen alignment pattern to a loose and disordered state with shorter fibers, contributing to reduced tumor stiffness and creating a TME more conducive to immune cell infiltration. In both orthotopic and metastatic mouse models of lung cancer, the inhalation of mscFv/siPD-L1@LNP boosts the infiltration of immune effector cells, including T cells, NK cells, and NKT cells, while reducing the presence of immunosuppressive cells in the TME, culminating in restrained tumor growth and prolonged overall survival. This study provides proof of concept for reshaping the immune-excluded and immunosuppressive TME through the inhalation of multimodal nucleic acid drugs, revitalizing antitumor immunity in lung cancer and supporting high feasibility for enhancing immune accessibility using inhaled gene therapy. We believe this approach could be widely applicable to various cancer types that encounter the common barriers of immune exclusion and immunosuppression during treatment. It may also enhance cancer immunotherapies that have shown limited success in solid tumors, such as chimeric antigen receptor T cell (CAR T) therapy.

Results

LNP maintains comparative properties before and after nebulization

An inhalable delivery platform that can withstand the shear forces generated during nebulization is essential for effective lung delivery. Building on our previously developed AA3-DLin ionizable lipid[29], we formulated LNPs for the co-delivery of siRNA and mRNA, using poloxamer 188 as an excipient to reduce viscosity and surface tension, thus improving nebulization efficiency[28]. The size distribution, hydrodynamic size, and polydispersity index (PDI) of mscFv/siPD-L1@LNP remained nearly unchanged after nebulization (Fig. 2a–c). mscFv/siPD-L1@LNP exhibited a slightly negative zeta potential of approximately −5.5 mV both before and after nebulization, which may help reduce electrostatic interactions with the negatively charged pulmonary mucus layer and minimize entrapment following inhalation (Supplementary Fig. 1). Both mscFv/siPD-L1@LNP and nebulized mscFv/siPD-L1@LNP exhibited similar encapsulation efficiencies of around 86% (Fig. 2d). The morphology of nanoparticles remained spherical and uniform, with consistent size before and after nebulization (Fig. 2e).

Next, we compared the intracellular behavior of LNP encapsulating mRNA and siRNA before and after nebulization in three different cancer cell lines. To investigate cellular uptake, mscFv/siPD-L1@LNP was labeled with Cy5 by substituting 18% of its cholesterol content with cholesterol-Cy5 during preparation. The results showed that mscFv/siPD-L1@LNP achieved nearly 100% cellular uptake both before and after nebulization, with similar amounts of internalized particles observed across all cell lines after four hours of incubation (Supplementary Fig. 2a, b and Fig. 2f). Endocytosis mechanism analysis revealed that LNP were internalized via multiple pathways, including caveolae-mediated endocytosis, macropinocytosis, and clathrin-mediated endocytosis, with clathrin-mediated endocytosis being the dominant route across all cancer cell types (Supplementary Fig. 3). Efficient lysosomal escape following cellular internalization is essential for the activity of mRNA or siRNA. We therefore assessed the lysosomal escape behavior of mscFv/siPD-L1@LNP using fluorescence imaging, which revealed that the LNP rapidly escaped from lysosomes (Supplementary Fig. 4). Using EGFP as a reporter gene, we evaluated the transfection efficiency and gene expression mediated by LNP and nebulized LNP. Both formulations effectively transfected the three cancer cell lines, with no statistically significant differences observed between them (Fig. 2g, h). By encapsulating each of the four siPD-L1 candidates in LNP and transfecting LLC cells, we screened for the candidate with the best knockdown performance (siPD-L1_3), which was then selected for use in both in vitro and in vivo experiments (Supplementary Fig. 5). In all tested cancer cells, mscFv/siPD-L1@LNP significantly downregulated PD-L1 expression, with nebulized mscFv/siPD-L1@LNP achieving a similar knockdown effect (Fig. 2i, j). To enhance the clinical relevance of the developed strategy, we also performed EGFP expression and PD-L1 knockdown assays in three human-derived lung cancer cell lines using both mscFv/siPD-L1@LNP and its nebulized form, which achieved transfection efficiencies exceeding 80% and significant PD-L1 silencing, with no statistically significant differences observed before and after nebulization (Supplementary Fig. 6). These results demonstrate that nebulization does not alter the physicochemical properties of LNP or its ability to mediate gene expression and silencing.

Design and validation of anti-DDR1 scFv mRNA

Elevated DDR1 levels in various cancers promote tumor progression by binding to collagen fibers and driving immune exclusion[9,10]. We hypothesize that blocking the binding of DDR1 ECD to collagen could disrupt fiber alignment and enhance immune infiltration, making DDR1 a promising target for cancer treatment. We first investigated the relationship between DDR1 expression and prognosis in lung cancer cohorts using the Kaplan–Meier plotter platform. Our analysis revealed that DDR1 overexpression was significantly associated with poorer survival outcomes ($P = 0.0055$) (Supplementary Fig. 7). Additionally, DDR1 expression at both the mRNA and protein levels was notably elevated in a murine lung cancer cell line and other tumor cell lines (Supplementary Fig. 8). These findings suggested the potential of targeting DDR1 signaling as a therapeutic strategy for lung cancer. Therefore, we designed an mRNA encoding anti-DDR1 scFv, which includes a signal sequence for secretion, a heavy chain variable region

https://doi.org/10.1038/s41467-025-63415-0

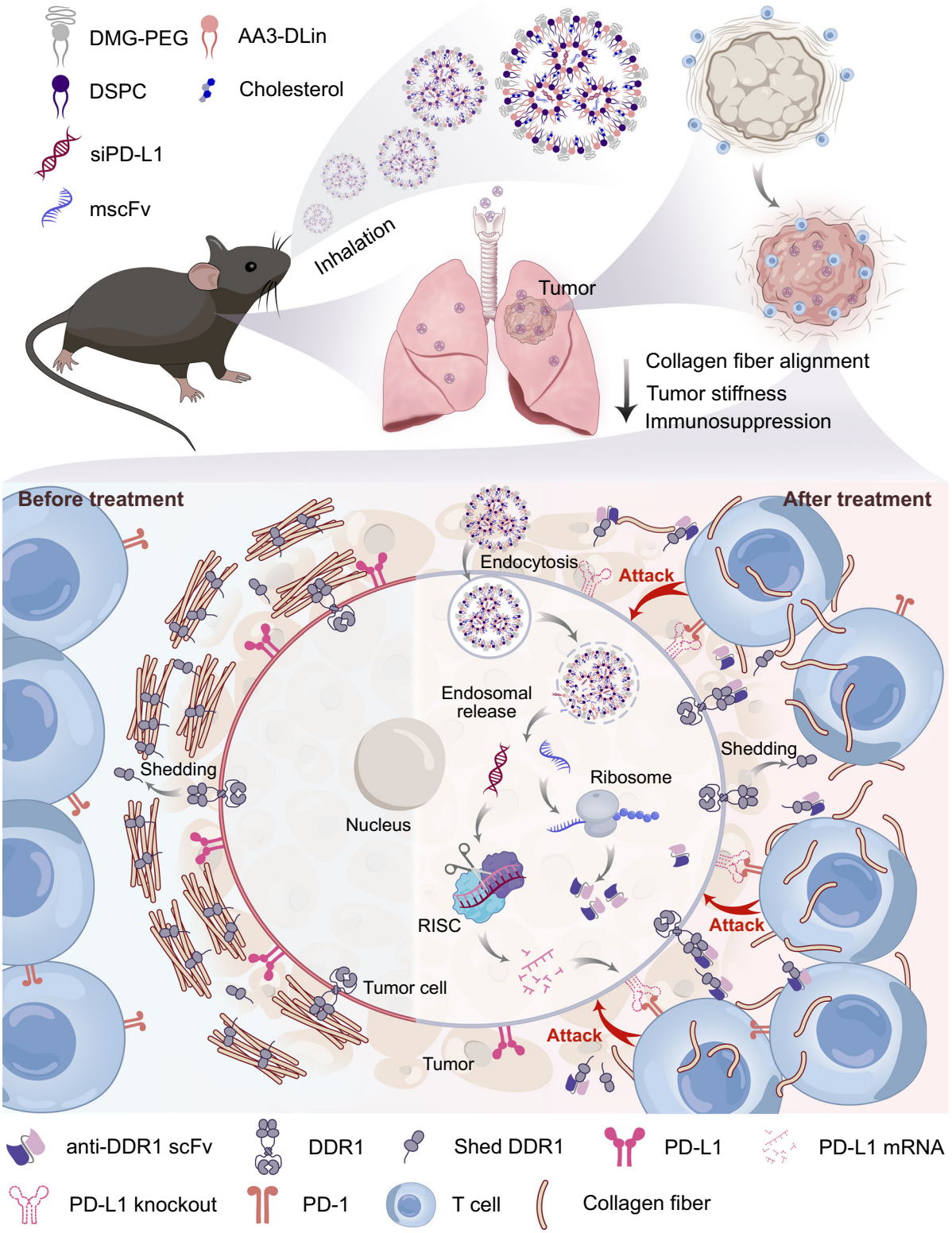

Fig. 1 | Schematic illustration of the antitumor immunity induced by the inhalation of mscFv/siPD-L1@LNP. Lung tumor-bearing mice are administered LNP co-delivering mscFv and siPD-L1 via inhalation. Following the internalization of LNP by cancer cells, mscFv and siPD-L1 are simultaneously released, translating into anti-DDR1 scFv and knocking down PD-L1 expression, respectively. The secreted anti-DDR1 scFv binds to DDR1 ECD, blocking its interaction with collagen, which disrupts collagen fiber alignment and reduces tumor stiffness. This creates a tumor microenvironment more favorable for immune effector cell infiltration. Consequently, antitumor immunity is enhanced by overcoming both the physical and immune barriers of the tumor's defense mechanisms.

(V_H), a light chain variable region (V_L), a poly-glycine-serine (G4S) linker connecting V_H and V_L, a FLAG tag for detection, and a 6×His-tag for purification (Supplementary Fig. 9a). After transfecting HEK293T cells with mscFv, we obtained anti-DDR1 scFv from the cell culture supernatant. Coomassie blue staining results and Western blot analysis confirmed the successful expression and purification of anti-DDR1 scFv (Supplementary Fig. 9b, c). The purified anti-DDR1 scFv was tested for binding affinity to DDR1 ECD using an ELISA assay, revealing an EC_{50} of

https://doi.org/10.1038/s41467-025-63415-0

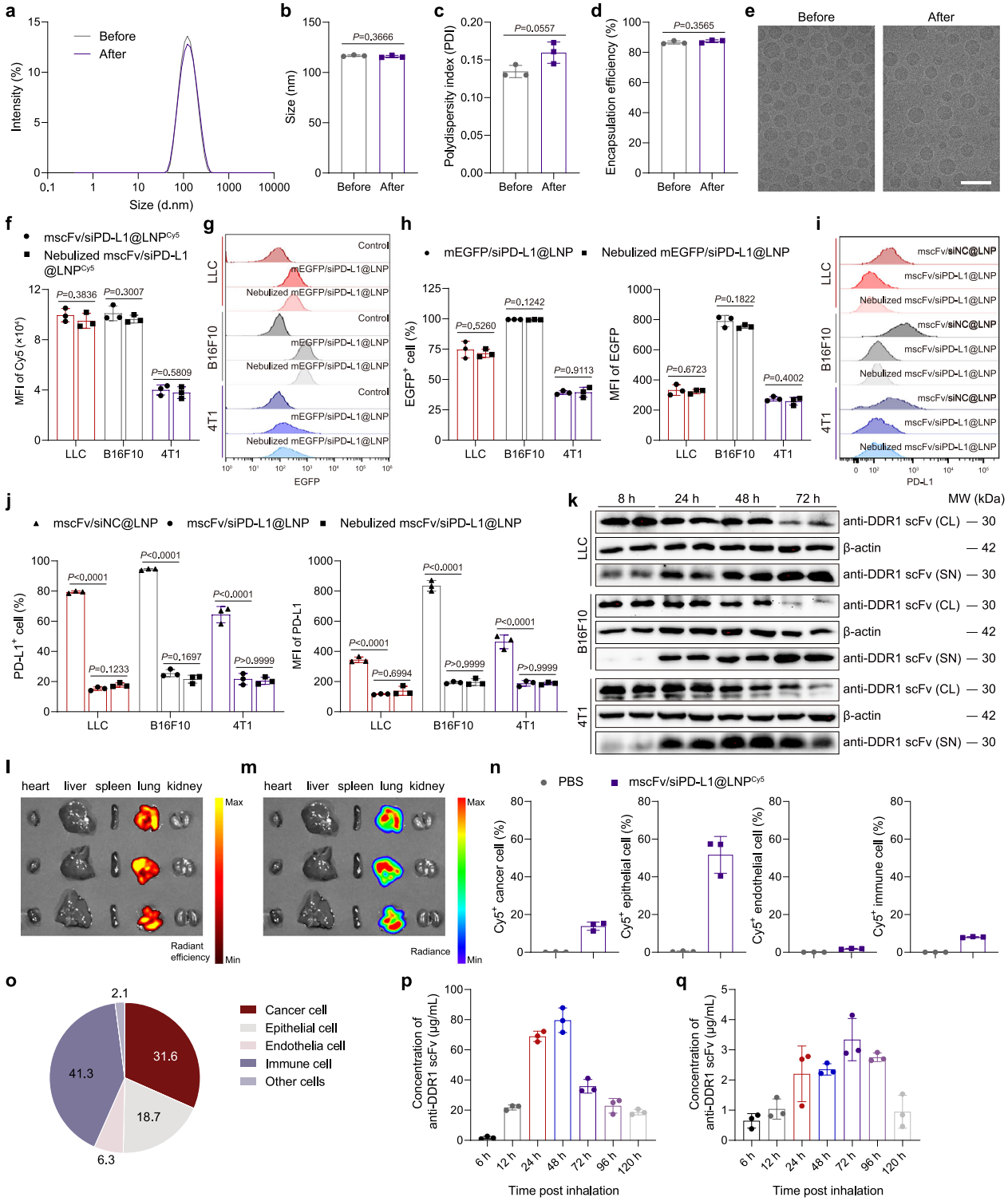

102.3 nM (Supplementary Fig. 10). mscFv was then encapsulated in LNP along with siPD-L1 and transfected into LLC, B16F10, and 4T1 cells to validate its expression (Fig. 2k). Anti-DDR1 scFv was detected in cell lysis 8 h post-transfection and persisted for over 72 h, though its levels were significantly reduced by the 72-h mark. In contrast, the level of secreted anti-DDR1 scFv in the supernatant continued to accumulate over the 72-h duration. These results confirm the effective expression of mscFv in cancer cells, with the in vitro expression kinetics offering guidance for scheduling administration in in vivo studies. Considering that normal lung cells, including epithelial cells and fibroblasts, also express DDR1[30], we further investigated whether mscFv affects their viability using the CCK-8 assay. BEAS-2B cells and primary mouse lung fibroblasts (MLF) were used as model cell types. Following treatment with mscFv@LNP at varying mRNA concentrations for 24 h, all groups showed comparable cell viability to the untreated control (Supplementary Fig. 11), indicating that the anti-DDR1 scFv encoded by mscFv was non-toxic to normal lung cells.

Inhalation of LNP results in effective lung delivery

The biodistribution of LNP following a single inhalation was examined. To assess in vivo deposition and mRNA translation, mLuc@LNP was labeled with Cy5 within the nanoparticle backbone and administered

Fig. 2 | Nebulized LNP enables efficient and desirable cellular uptake, transfection, gene silencing, and gene expression both in vitro and in vivo. a–e Size distribution (**a**), particle size ($n = 3$ independent samples) (**b**), polydispersity index (PDI) ($n = 3$ independent samples) (**c**), encapsulation efficiency ($n = 3$ independent samples) (**d**), and representative cryo-TEM images (**e**) of mscFv/siPD-L1@LNP before and after nebulization. Scale bar: 100 nm. Data were representative of three independent experimental replicates with similar results. **f** Mean fluorescence intensity (MFI) of LLC, B16F10, and 4T1 cells treated with Cy5-labled mscFv/siPD-L1@LNP or nebulized mscFv/siPD-L1@LNP for 4 h ($n = 3$ biologically independent samples). **g**,**h** Representative flow cytometric histogram (**g**) and relative quantifications of EGFP-positive cells and MFI of EGFP (**h**) in LLC, B16F10, and 4T1 cells following treatment with mEGFP/siPD-L1@LNP or nebulized mEGFP/siPD-L1@LNP for 24 h ($n = 3$ biologically independent samples). **i**,**j** Representative flow cytometric histogram (**i**) and relative quantifications of PD-L1-positive cells and MFI of PD-L1 (**j**) in LLC, B16F10, and 4T1 cells following treatment with mscFv/siPD-L1@LNP or nebulized mscFv/siPD-L1@LNP for 48 h ($n = 3$ biologically independent samples). **k** LNP-mediated mscFv expression in cell lysis (CL) and supernatant (SN) at different time points following transfection of LLC, B16F10, and 4T1 cells. Data were representative of three independent experimental replicates with similar results. **l**, **m** IVIS imaging of Cy5-labled LNP signals (**l**) and luciferase signals (**m**) in major organs of mice 6 h after inhalation of mLuc@LNP^{Cy5} ($n = 3$ mice). **n** Percentage of different cell subtypes internalizing Cy5-labeled mscFv/siPD-L1@LNP 6 h post-inhalation ($n = 3$ mice). **o** Uptake distribution of mscFv/siPD-L1@LNP^{Cy5} across different cell subtypes 6 h post-inhalation ($n = 3$ mice). Flow cytometry gating strategies are shown in Supplementary Fig. 26. **p**, **q** Concentration of DDR1 scFv in lung homogenate (**p**) and bronchoalveolar lavage fluid (**q**) at different time points following a single-dose inhalation of mscFv/siPD-L1@LNP ($n = 3$ mice). Results are presented as mean ± s.d. Statistical analysis was performed using two-tailed unpaired Student's *t*-test (**b**–**d**, **f**, **h**) or by one-way ANOVA with Bonferroni's multiple comparisons test (**j**). *P* values as indicated. Source data are provided as a Source Data file.

to C57BL/6 mice via inhalation at a dose of 0.25 mg/kg. Six hours after inhalation, major organs were collected and analyzed for Cy5 and luciferase signals, revealing that both LNP accumulation and luciferase expression were restricted to the lungs (Fig. 2l, m and Supplementary Fig. 12). To identify the cell subtypes internalizing LNP, mice bearing orthotopic LLC lung tumors were treated with mscFv/siPD-L1@LNP^{Cy5}. Six hours later, the tumor-bearing lungs were digested and analyzed via flow cytometry. Key lung cell types, including cancer cells, epithelial cells, endothelial cells, and immune cells, were evaluated, showing that 13.8, 51.7, 1.8, and 8.0% of these respective cells internalized LNP (Fig. 2n). Cancer cells and immune cells were the primary cell types taking up LNP, internalizing 31.6 and 41.3% of the total mscFv/siPD-L1@LNP^{Cy5}, respectively (Fig. 2o). Functional mRNA expression in vivo was then assessed. Mice were administered mscFv/siPD-L1@LNP by inhalation, and anti-DDR1 scFv levels were measured at various time points. As shown in Fig. 2p, q, anti-DDR1 scFv was detectable in both lung homogenates and bronchoalveolar lavage fluid (BALF), with sustained in vivo expression for at least 120 h. Anti-DDR1 scFv concentrations in lung homogenates peaked at 48 h post-inhalation, while in BALF, peak levels were reached at 72 h, likely due to delayed secretion. These results suggested that a dosing frequency of every 2 days in in vivo studies could sustain high levels of anti-DDR1 scFv in the lung tumor microenvironment.

mscFv/siPD-L1@LNP induces strong antitumor effects in vitro

To evaluate the in vitro antitumor efficacy of mscFv/siPD-L1@LNP, a co-culture system of tumor cells and T cells was established. LLC, B16F10, and 4T1 cells were pretreated with various formulations and then co-cultured with activated $CD8^+$ T cells for 24 h. Tumor cell apoptosis was measured by flow cytometry after staining with Annexin V/propidium iodide (PI) (Fig. 3a–d). $CD8^+$ T cell-mediated tumor killing was modest in the control and LNP groups, which could be attributed to the immune escape mechanisms facilitated by PD-1/PD-L1 signaling. Treatment with mscFv alone induced certain cancer cell apoptosis, possibly because the DDR1/collagen binding also activates anti-apoptotic signaling pathways in cancer cells[31]. After simultaneously downregulating PD-L1 and blocking DDR1 signaling, the mscFv/siPD-L1@LNP group exhibited the highest levels of apoptotic tumor cells. We further analyzed the cytokine-producing capacity of $CD8^+$ T cells in the co-culture system (Fig. 3e–g). Treatment with mscFv/siPD-L1@LNP significantly increased the release of granzyme B, IFN-γ, and TNF-α by $CD8^+$ T cells, demonstrating restored T cell function and enhanced cytotoxicity against cancer cells. The levels of cytokines released into the cell culture supernatant were measured by Western blot, revealing increased secretion of pro-inflammatory cytokines, including TNF-α, IL-1β, and IL-6, along with a reduced production of the immunosuppressive cytokine IL-10 following treatment with mscFv/siPD-L1@LNP (Fig. 3h). PD-L1 and DDR1 are known to promote tumor cell migration[32,33], so we also investigated the effects of different treatments on this process. Simultaneous blockade of PD-L1 and DDR1 signaling led to the greatest inhibition of cancer cell migration (Supplementary Fig. 13).

Inhalation of mscFv@LNP alleviates immune exclusion by rearranging collagen fibers and reducing tumor stiffness

We then evaluated the in vivo function of the anti-DDR1 scFv designed in this study following inhalation of mscFv@LNP at low or high doses. An orthotopic lung cancer mouse model was first established by surgically implanting 2×10^5 LLC-Luc cells into the left lung lobe of C57BL/6 mice. The procedure did not cause any complications, as indicated by unchanged pulmonary function before and after surgery (Supplementary Fig. 14). mscFv@LNP was administered every 2 days for a total of six inhalations (Supplementary Fig. 15a). Second harmonic generation (SHG) imaging revealed that, without treatment, the collagen fibers within the tumor were highly aligned (Fig. 4a), forming a barrier that impeded immune cell infiltration. Treatment with mscFv@LNP at doses of 0.5 or 1 mg/kg disrupted fiber alignment to varying degrees, with the 1 mg/kg dose resulting in the fibers becoming loose and disordered. The degree of fiber alignment, quantified by the coefficient of alignment, was significantly reduced to 75.1 and 48.4% of the PBS-treated controls following treatment with mscFv@LNP at doses of 0.5 and 1 mg/kg, respectively (Fig. 4b). In addition, the length of collagen fibers was markedly shortened in the 1 mg/kg group (Fig. 4c). The ability of mscFv@LNP to alter collagen fiber configuration was also verified in a pulmonary metastasis model of breast cancer, established by intravenously injecting 4T1-Luc cells. Similarly, inhalation of 1 mg/kg mscFv@LNP caused the collagen fibers to shift from dense and aligned to loose and disordered, with a significant decrease in both the coefficient of alignment and fiber length compared to the PBS group (Fig. 4d–f). Aligned collagen fibers have been shown to increase tissue matrix stiffness[34]. Therefore, we assessed tumor stiffness using atomic force microscopy. The stiffness of tumors decreased in a dose-dependent manner following mscFv inhalation in both the orthotopic LLC tumor (Fig. 4g, h) and the breast cancer lung metastasis model (Fig. 4i, j), demonstrating that mscFv@LNP significantly altered the mechanical properties of the tumor tissue.

Based on these findings, we next investigated the impact of mscFv@LNP on immune infiltration. A dose gradient ranging from 0.05 to 1.25 mg/kg was administered to mice bearing LLC lung tumors, resulting in a dose-dependent control of tumor growth (Supplementary Fig. 15b). The concentration of anti-DDR1 scFv in the tumor tissue was measured by ELISA, which showed a direct correlation with the inhalation dose of mscFv@LNP (Supplementary Fig. 16). The number of infiltrated immune cells, including total immune cells, $CD4^+$ T cells, $CD8^+$ T cells, NK cells, and NKT cells within TME was analyzed by flow cytometry (Fig. 4k–o). An increase in the presence of all tested immune

https://doi.org/10.1038/s41467-025-63415-0

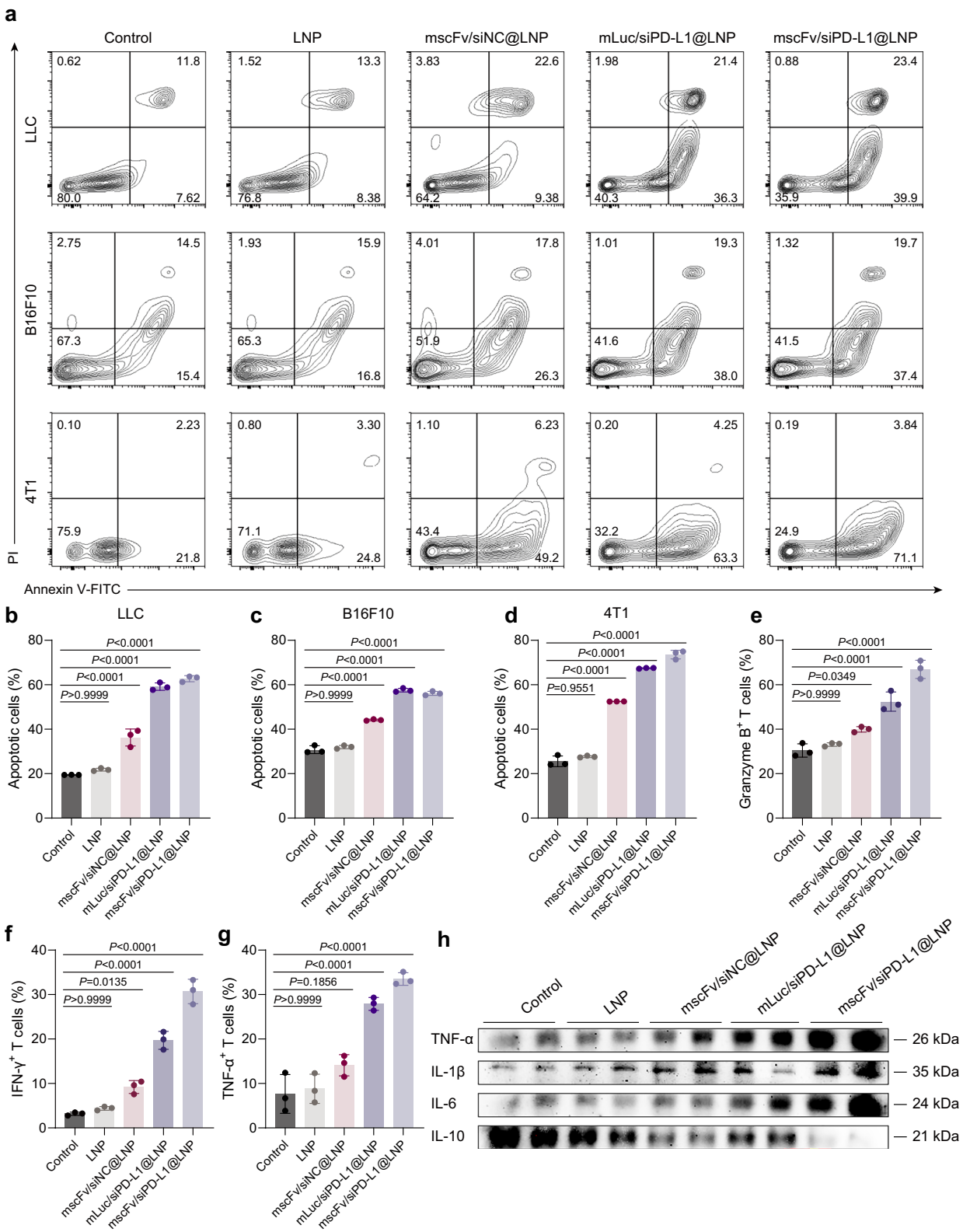

Fig. 3 | mscFv/siPD-L1@LNP demonstrates excellent antitumor effects in vitro. **a**–**d** Representative flow cytometric analysis profiles (**a**) and relative quantifications of apoptotic LLC cells (**b**), B16F10 cells (**c**), and 4T1 cells (**d**) following co-culture with activated $CD8^+$ T cells for 24 h ($n = 3$ biologically independent samples). The cancer cells were pretreated with the specified formulations four hours prior to co-culturing with T cells. **e**–**g** Quantification of granzyme B^+ (**e**), IFN-γ^+ (**f**), and TNF-α^+ (**g**) T cells following co-culture of LLC cells with $CD8^+$ T cells using flow cytometry ($n = 3$ biologically independent samples). **h** Determination of TNF-α, IL-1β, IL-6, and IL-10 levels in the supernatant of co-cultured LLC cells and $CD8^+$ T cells. Data were representative of three independent experimental replicates with similar results. Results are presented as mean ± s.d. Statistical analysis was performed using one-way ANOVA with Bonferroni's multiple comparisons test (**b**–**g**). *P* values as indicated. Source data are provided as a Source Data file.

https://doi.org/10.1038/s41467-025-63415-0

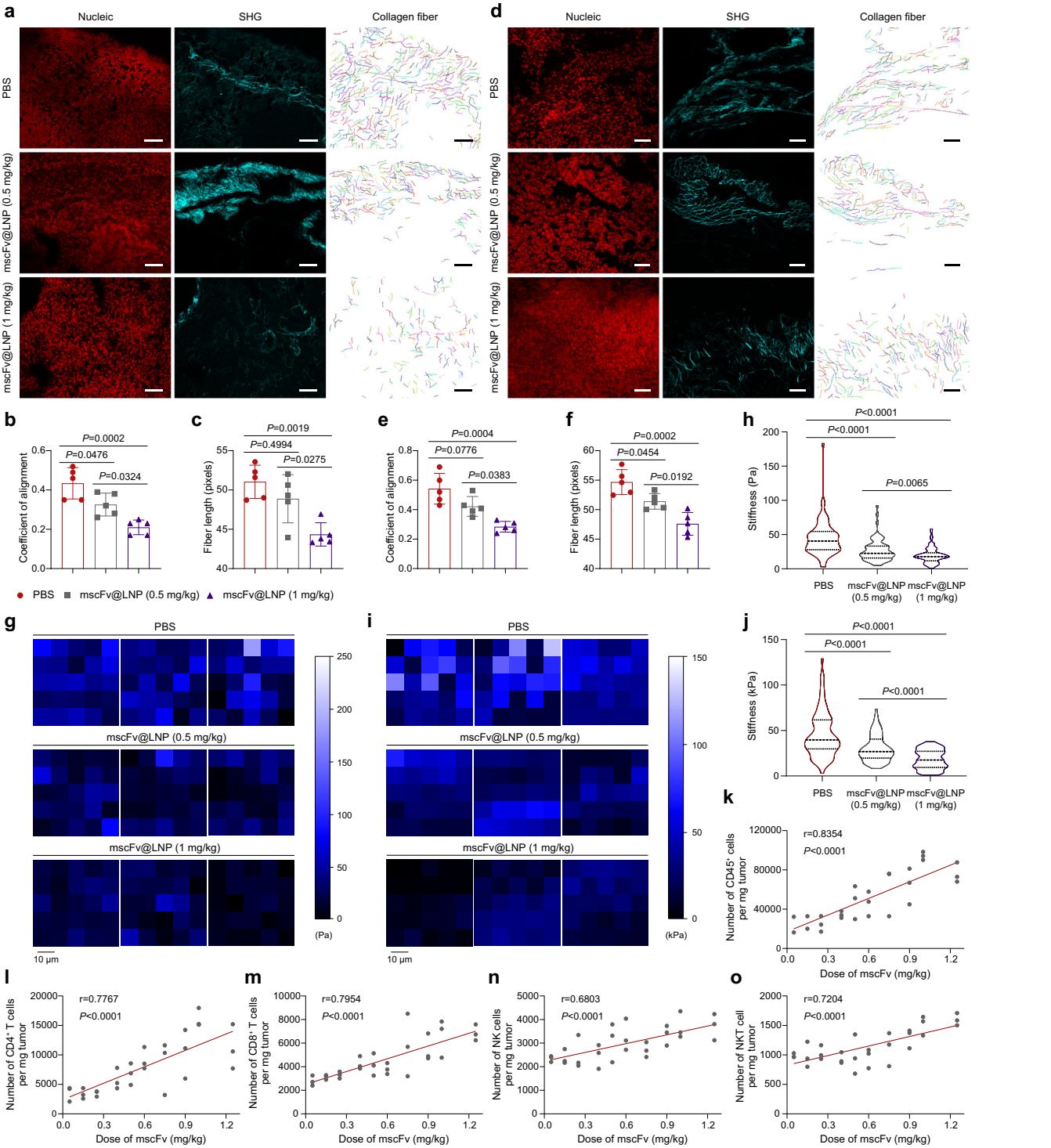

cell types was observed with escalating doses of mscFv, indicating a strong correlation between immune cell infiltration and the dose of mscFv. Collectively, these data demonstrate that inhalation of mscFv effectively disrupts aligned collagen fibers within lung tumor tissues and reduces tumor stiffness, leading to the reversal of immune exclusion and enhanced infiltration of various immune effector cells.

Inhalation of mscFv/siPD-L1@LNP inhibits the progression of orthotopic lung tumors

We assessed the antitumor effects of the inhaled therapy in a mouse model of orthotopic lung cancer. The mice were administered PBS, empty LNP, mscFv/siNC@LNP, mEGFP/siPD-L1@LNP, or mscFv/siPD-L1@LNP via inhalation on days 6, 8, 10, 12, 14, and 16 (Fig. 5a). Tumor progression during treatment was monitored using IVIS Spectrum imaging, and tumor burden was quantified by measuring the intensity of the luciferase signal (Fig. 5b, c). Tumors grew rapidly in the PBS and LNP groups without drug intervention. Treatment with mscFv/siNC@LNP and mEGFP/siPD-L1@LNP significantly delayed tumor progression, while the inhalation of mscFv/siPD-L1@LNP achieved the most favorable therapeutic outcomes among the five groups. One day after the final treatment, tumor-bearing lungs from each group were collected and examined by H&E staining (Fig. 5d). Compared to the

Fig. 4 | mscFv@LNP promotes immune infiltration by disrupting collagen fiber alignment and reducing tumor stiffness. a Representative images of PI-stained nuclei, SHG, and collagen fiber individualization in LLC lung tumors with the indicated treatments. Scale bar: 50 μm. Data were representative of three independent experimental replicates with similar results. **b**,**c** Coefficient of alignment (**b**) and length (**c**) of collagen fibers in LLC lung tumors following different treatments ($n = 5$ mice). **d** Representative images of PI-stained nuclei, SHG, and collagen fiber individualization in 4T1 metastatic lung tumors with indicated treatments. Scale bar: 50 μm. Data were representative of three independent experimental replicates with similar results. **e**–**f** Coefficient of alignment (**e**) and length (**f**) of collagen fibers in 4T1 metastatic lung tumor following different treatments ($n = 5$ mice). **g**, **h** Stiffness map (**g**) and quantification of tissue stiffness (**h**) in LLC lung tumors with indicated treatments ($n = 3$ mice). Data were representative of three independent experimental replicates with similar results. **i-j**, Stiffness map (**i**) and quantification of tissue stiffness (**j**) in 4T1 metastatic lung tumors with indicated treatments ($n = 3$ mice). Data were representative of three independent experimental replicates with similar results. **k**–**o** Correlation analysis of mscFv dose and the infiltration of $CD45^+$ immune cells (**k**), $CD4^+$ T cells (**l**), $CD8^+$ T cells (**m**), NK cells (**n**), and NKT cells (**o**) into LLC lung tumors ($n = 3$ mice for each dosage). Flow cytometry gating strategies are shown in Supplementary Fig. 27. Results are presented as mean ± s.d. Statistical analysis was performed using one-way ANOVA with Bonferroni's multiple comparisons test (**b**, **c**, **e**, **f**), Brown–Forsythe and Welch ANOVA tests with Games–Howell's multiple comparisons test (**h**, **j**), or Pearson correlation analysis with a two-tailed test (**k**–**o**). *P* values as indicated. Source data are provided as a Source Data file.

PBS and LNP groups, treatment with either mscFv alone, siPD-L1 alone, or their combination effectively controlled tumor growth, with the mscFv/siPD-L1@LNP treatment showing the most significant tumor regression, as evidenced by the reduced tumor areas. We recorded the body weight of mice from different groups until day 27 post-tumor inoculation. A significant decrease in body weight was observed only in the PBS and empty vehicle groups (Fig. 5e), revealing aggressive tumor progression. In parallel, lung weight measurements revealed a significant decrease in the lungs of the mscFv/siPD-L1@LNP group compared to the other four groups, indicating minimal tumor growth in this group (Fig. 5f). The survival of mice from different groups was monitored until day 60 post-tumor inoculation (Fig. 5g). All mice in the PBS and LNP groups died by day 31, with median survival times of 23 and 25.5 days, respectively. Although treatment with siPD-L1 alone inhibited tumor growth during the treatment cycle, these effects were not durable, as indicated by the moderate impact on extending mouse survival. In the mscFv/siNC@LNP group, median survival was significantly prolonged to 34 days. Treatment with mscFv/siPD-L1@LNP further extended the median survival time to 54 days, with 50% of the mice still alive at the end of the monitoring period. These data suggest that inhalation of mscFv/siPD-L1@LNP can effectively hinder the advancement of orthotopic lung cancer, demonstrating significantly better therapeutic effects compared to mscFv or siPD-L1 therapy alone. The therapeutic efficacy of inhaled mscFv/siPD-L1@LNP was also evaluated in a male mouse model of LLC-induced orthotopic lung cancer, using the same tumor implantation method and administration regimen (Supplementary Fig. 17). Consistently, treatment with mscFv/siPD-L1@LNP significantly inhibited tumor growth and prolonged overall survival, indicating that the therapeutic effectiveness of this strategy is not sex-dependent. Additionally, we performed TUNEL staining on lung tissue sections from mice treated with mscFv/siPD-L1@LNP to assess whether the treatment induced unintended apoptosis in DDR1-expressing normal tissues (Supplementary Fig. 18). While DDR1 expression was detected in both tumor and lung regions, apoptotic signals were predominantly localized to tumor areas, with minimal apoptosis observed in normal lung tissues, supporting that this therapy safely inhibited tumor progression without causing toxicity to normal tissues.

Inhalation of mscFv/siPD-L1@LNP drives TME reconfiguration in orthotopic lung tumors

We first examined gene expression and silencing in tumor-bearing mice as a basis for assessing the potential of mscFv/siPD-L1@LNP to reshape TME. The expression of anti-DDR1 scFv was confirmed by immunofluorescent staining, revealing its production after inhalation of mscFv/siNC@LNP or mscFv/siPD-L1@LNP, with no expression observed in the other three groups (Supplementary Fig. 19a). Collagen fiber rearrangement mediated by anti-DDR1 scFv was analyzed using picrosirius red staining. Treatment with mscFv resulted in disordered and shorter collagen fibers compared to the other groups (Fig. 5h, i). Immunofluorescent staining and Western blot analysis of PD-L1 demonstrated PD-L1 downregulation in the treatment groups containing siPD-L1 (Fig. 5j and Supplementary Fig. 20).

Next, we investigated alterations in the TME following inhalation treatment with mscFv/siPD-L1@LNP in an orthotopic LLC model (Fig. 6a). The different immune cell populations within the tumors were characterized and analyzed using flow cytometry. The proportion of $CD8^+$ T cells increased following treatment with mscFv/siNC@LNP or mLuc/siPD-L1@LNP compared to the PBS or placebo groups. The synergistic effects of mscFv and siPD-L1 were evident in the significantly higher frequency of $CD8^+$ T cells in the mscFv/siPD-L1@LNP group compared to the other groups (Fig. 6b). The blockade of PD-1/PD-L1 signaling is known to alleviate immunosuppression in the TME[35]. Therefore, we examined the levels of immunosuppressive cells in tumors after treatment. The frequency of the primary immunosuppressive cell types, including regulatory T cells (Tregs) and myeloid-derived suppressor cells (MDSCs), was significantly reduced in the treatment regimen that included siPD-L1 (Fig. 6c, d), indicating that downregulation of PD-L1 expression via RNAi effectively reversed immunosuppression. The capacity of $CD8^+$ T cells to secrete IFN-γ was evaluated (Fig. 6e). In the mscFv/siNC@LNP and mLuc/siPD-L1@LNP groups, the proportion of $CD8^+IFN\text{-}\gamma^+$ T cells increased by 2.3-fold and 2.5-fold, respectively, compared to the PBS group. Notably, a 4-fold increase in the frequency of $CD8^+IFN\text{-}\gamma^+$ T cells was observed in the mscFv/siPD-L1@LNP group compared to the PBS group. Meanwhile, the proliferative capacity of $CD8^+$ T cells was significantly enhanced, as indicated by the markedly higher proportion of $CD8^+Ki67^+$ T cells in the mscFv/siPD-L1@LNP group compared to the other groups (Fig. 6f). To verify the enhanced immune infiltration in lung tumors achieved by the developed inhaled therapy, we measured the number of total immune cells ($CD45^+$ cells), $CD4^+$ T cells, and $CD8^+$ T cells within the tumors by flow cytometry and immunofluorescent staining (Fig. 6g–i and Supplementary Fig. 9b, c). In the PBS and LNP groups, immune infiltration levels were low but showed a slight increase following treatment with mLuc/siPD-L1@LNP. However, the inclusion of mscFv in the inhaled formulation significantly boosted the number of immune cells in the TME. Specifically, treatment with mscFv/siNC@LNP increased the number of $CD45^+$ cells, $CD4^+$ T cells, and $CD8^+$ T cells by fourfold, 4.2-fold, and 4.9-fold, respectively. The mscFv/siPD-L1@LNP treatment further enhanced these increases by fourfold, 4.3-fold, and 7.9-fold, respectively, compared to the PBS group. Additionally, cytokine levels in the TME were quantified by ELISA. The concentrations of immunostimulatory cytokines, including IFN-γ, IL-2, IL-12p70, and TNF-α, were significantly elevated following mscFv/siPD-L1@LNP treatment compared to the other four groups (Fig. 6j–m). Conversely, mscFv/siPD-L1@LNP treatment substantially reduced the level of IL-10, a potent immunosuppressive cytokine (Fig. 6n and Supplementary Fig. 19d). While enhanced immune infiltration and pro-inflammatory cytokine secretion were noted in the pulmonary TME, serum levels of pro-inflammatory cytokines remained similar across treatment groups (Supplementary

https://doi.org/10.1038/s41467-025-63415-0

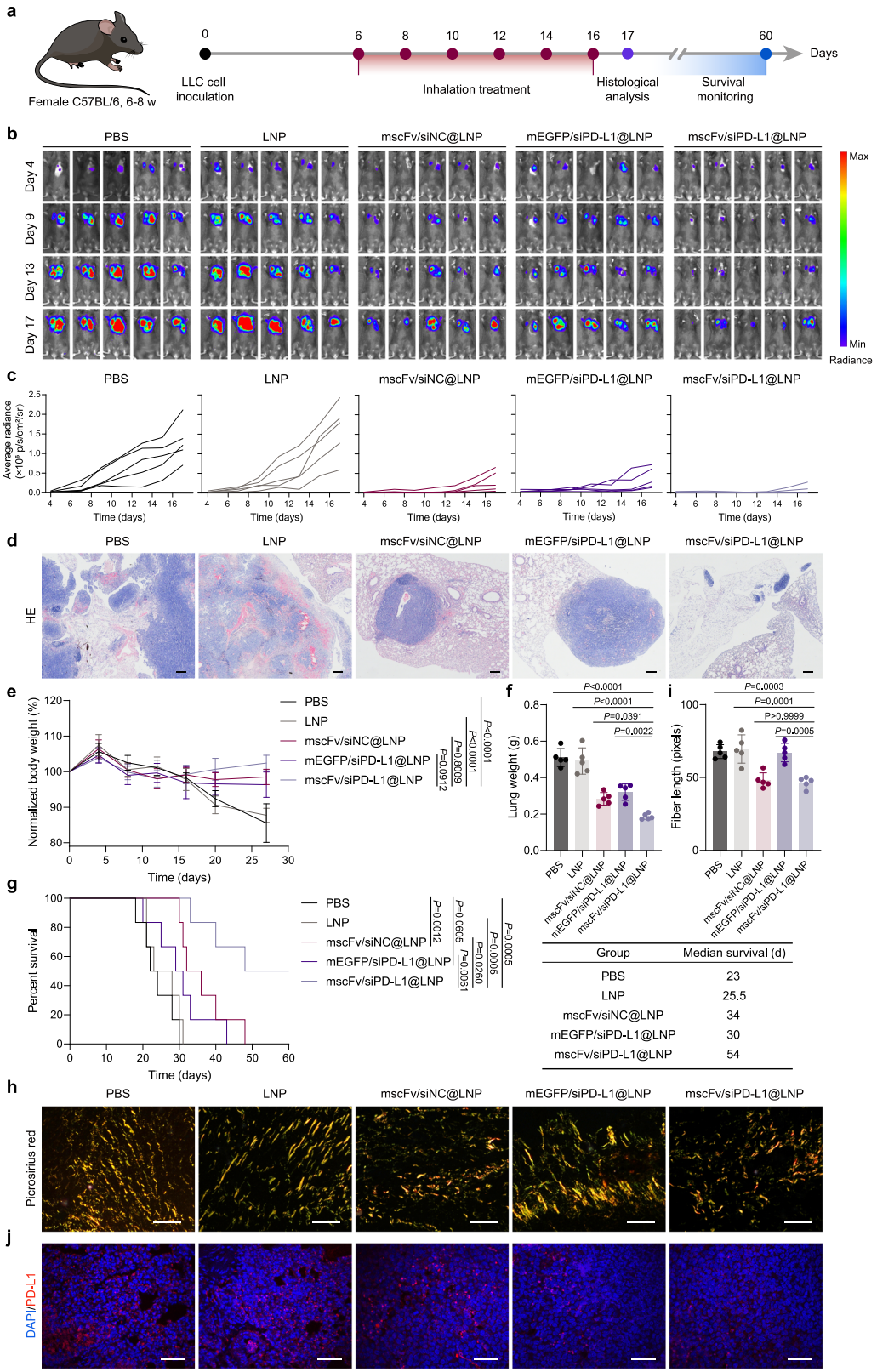

Fig. 21). This indicates that pulmonary delivery of mRNA/siRNA-LNPs resulted in minimal systemic cytokine production, thus mitigating potential safety concerns. Collectively, the inhalation of mscFv/siPD-L1@LNP effectively reprogrammed the hostile lung TME by simultaneously boosting immune infiltration and reversing immunosuppression, thereby creating a more favorable environment for a stronger immune response against cancer cells.

Inhalation of mscFv/siPD-L1@LNP controls the progression of metastatic lung cancers through dual reconfiguration of the TME

To determine if the tumor suppression observed with the developed inhalation strategy is limited to orthotopic lung cancers, we established a mouse model of pulmonary metastasis of breast cancer by intravenous injection of 1×10^5 4T1-Luc cells and administered

Fig. 5 | Inhalation of mscFv/siPD-L1@LNP retards tumor progression in an orthotopic mouse model of lung cancer. a Schematic illustration of the inoculation of LLC-Luc cells via orthotopic injection and the following treatment and analysis schedules. **b**,**c** In vivo bioluminescence images reveal the tumor burden in mice receiving different treatments at indicated time points (**b**) and quantification of luciferase signals from each individual mouse (**c**) ($n = 5$ mice). **d** Representative H&E-stained lung sections from mice following indicated treatments on day 17. Scale bar: 200 μm. Data were representative of three independent experimental replicates with similar results. **e** Body weight of mice from different treatment groups, normalized to day 0 ($n = 5$ mice). **f** Lung weight of mice from different treatment groups serves as a proxy for tumor burden ($n = 5$ mice). **g** Kaplan–Meier survival curves and median survival time of tumor-bearing mice ($n = 6$ mice). **h** Representative images of picrosirius red-stained lung tumor, examined under polarized light microscopy. Scale bar: 100 μm. Data were representative of three independent experimental replicates with similar results. **i** Quantification of collagen fiber length ($n = 5$ mice). **j** Representative immunofluorescence images for PD-L1 expression in lung tumor areas. Scale bar: 50 μm. Data were representative of three independent experimental replicates with similar results. Results are presented as mean ± s.d. Statistical analysis was performed using one-way ANOVA with Bonferroni's multiple comparisons test (**e**,**f**, **i**) or by log-rank (Mantel–Cox) test (**g**). *P* values as indicated. Source data are provided as a Source Data file.

different formulations via inhalation, with a total of six treatments (Fig. 7a). The IVIS images and tumor signal intensity curve revealed substantial tumor growth in the PBS and LNP groups (Fig. 7b, c), highlighting the aggressiveness of 4T1 breast cancer lung metastasis. The tumor inhibition by mEGFP/siPD-L1@LNP treatment was modest, showing some effect during the early phase of tumor development, likely due to the resistance of 4T1 breast cancer to ICB therapy[36,37]. Inhalation of mscFv/siNC@LNP suppressed tumor growth, and this therapeutic effect was further enhanced in mice treated with mscFv/siPD-L1@LNP, which resulted in the most pronounced tumor inhibition among the treatment groups. To assess tumor burden, tumor-bearing lungs were excised on day 18 post-tumor inoculation for morphological observation and H&E staining, with the number of metastatic foci also quantified (Fig. 7d–f and Supplementary Fig. 22). Consistent with the IVIS results, lungs from the PBS and LNP vehicle groups displayed dense metastatic foci, with a slight reduction observed in the mEGFP/siPD-L1@LNP group. While mscFv alone significantly reduced tumor burden, the combination therapy resulted in the fewest metastatic foci in the lung tissues. Since tumor growth in the lung increased lung weight, the lung weights followed a similar pattern to the number of metastatic foci across the five groups (Fig. 7g). The rapid tumor growth in the PBS, LNP, and mEGFP/siPD-L1@LNP groups resulted in a significant decrease in body weight, whereas the average normalized body weight of mice in the treatment groups containing mscFv remained above 100% at 20 days post-tumor implantation (Supplementary Fig. 23). The rapid tumor progression culminated in the death of all animals within 31 days in the PBS, LNP, and mEGFP/siPD-L1@LNP groups (Fig. 7h). Treatment with mscFv/siNC@LNP extended median survival to 35 days, while mscFv/siPD-L1@LNP recipients showed significantly longer survival compared to other groups, owing to its synergistic therapeutic effects.

We further investigated changes in the TME after treatment. The presence of immunosuppressive cells, including Tregs and MDSCs, was analyzed by flow cytometry, revealing that PD-L1 downregulation via the siRNA strategy effectively alleviated immunosuppression (Fig. 7i, j). The number of total immune cells, $CD4^+$ and $CD8^+$ T cells, as well as NK and NKT cells that directly kill cancer cells, was assessed (Fig. 7k–o). By disrupting collagen fiber alignment, treatment with mscFv/siNC@LNP or mscFv/siPD-L1@LNP significantly reduced immune exclusion and promoted the infiltration of these immune cells. Overall, mLuc/siPD-L1@LNP achieved similar effects in reversing immunosuppression as mscFv/siPD-L1@LNP, while mscFv/siNC@LNP had comparable effects in relieving immune exclusion. However, the therapeutic efficacy of mscFv/siPD-L1@LNP was significantly superior to both, highlighting that addressing both insufficient immune infiltration and immunosuppression is crucial for effective lung cancer treatment.

In vivo biosafety evaluation

To assess in vivo toxicity following inhalation of mscFv/siPD-L1@LNP, we administered six doses to healthy mice. Major organs and blood samples were collected 24 h after the final inhalation for evaluation (Supplementary Fig. 24a). H&E staining of major organs, including the heart, liver, spleen, and kidneys, showed no lesions, histopathological injuries, or abnormalities caused by the inhalation of mscFv/siPD-L1@LNP (Supplementary Fig. 24b). Particular attention was given to lung structure, where LNPs primarily accumulate (Supplementary Fig. 24c). The alveoli, large airways, and small airways remained intact and clear, with no signs of inflammation or damage in any of the groups. The potential side effects of mscFv/siPD-L1@LNP on liver function, heart function, kidney function, and glycometabolism were assessed through serum biochemical analysis, which showed no statistically significant differences among the treatment groups for any of the tested parameters (Supplementary Fig. 25a). Hematological analysis also confirmed no impact on blood components or function (Supplementary Fig. 25b). These findings suggest a favorable biosafety profile for mscFv/siPD-L1@LNP, supporting its potential for further preclinical or clinical investigation.

Discussion

The therapeutic efficacy of immunotherapies for solid tumors is often constrained by the hostile TME shaped by cancer cells. Particularly, physical barriers within the ECM limit T cell infiltration, while the highly immunosuppressive conditions further impair the function and proliferation of infiltrating immune effector cells[14,38,39]. These challenges have contributed to the unsatisfactory outcomes seen in clinical trials of CAR T therapy for solid tumors[40]. However, addressing only one of these issues is insufficient to restore antitumor immunity[41], as evidenced by the broad resistance to ICB therapy, which disrupts immunosuppressive mechanisms but is largely hindered by poor T cell infiltration[42]. Here, we propose a combinational RNA-LNP strategy that integrates mRNA-mediated antibody therapy with RNAi to reconstruct the immune-excluded and immunosuppressive TME. By delivering different RNA payloads, the LNP enables simultaneous modulation of different tumorigenic signaling pathways through a single administration, offering an effective approach to initiating a cascade in the cancer-immunity cycle. In this study, mscFv and siPD-L1 were co-delivered using an inhalable LNP with the goal of enhancing immune infiltration while simultaneously reversing the immunosuppressive TME, thereby strengthening antitumor response in lung cancer treatment.

DDR1 is frequently upregulated in various cancers and is considered a key mechanism in initiating immune exclusion during tumor progression. DDR1 ECD sculpts the ECM by binding to collagen and promoting collagen fiber alignment, forming a barrier that obstructs T cell infiltration[9–11]. Although no drugs targeting DDR1 have been approved to date, a clinical trial is currently underway for PRTH-101, an anti-DDR1 monoclonal antibody[43]. To overcome immune exclusion and enhance T cell infiltration, we designed an anti-DDR1 scFv and its encoding mRNA. Compared to full-length antibodies, scFvs offer smaller size, better tumor penetration, and enhanced pharmacokinetic properties[44]. Once administered, mscFv could be translated into anti-DDR1 scFv, which neutralizes DDR1 ECD. In mouse models of both orthotopic and metastatic lung cancers, treatment with mscFv caused collagen fibers to shift from a dense, aligned state to a loose, disordered arrangement. These alterations subsequently led to changes

https://doi.org/10.1038/s41467-025-63415-0

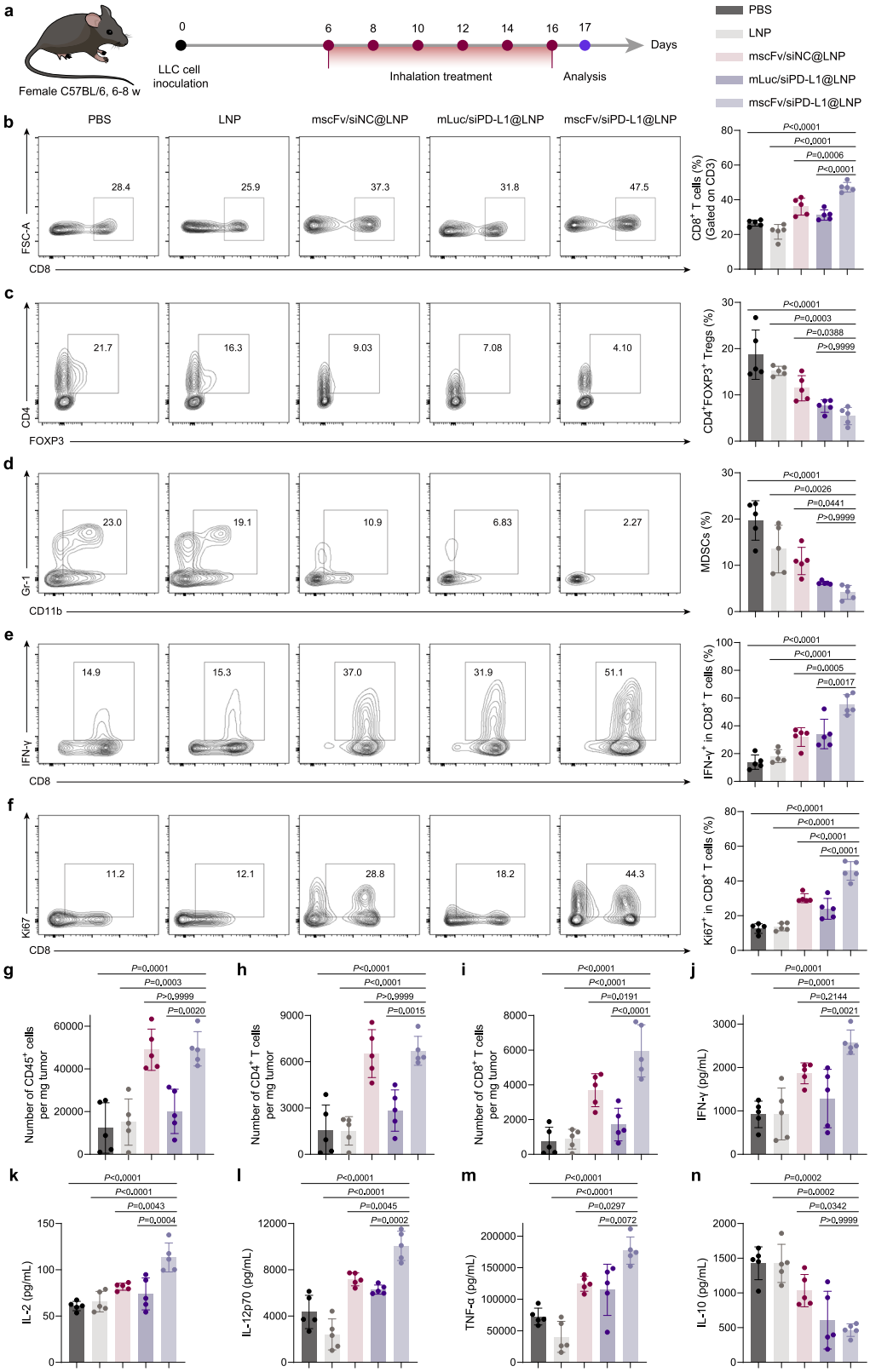

Fig. 6 | Inhalation of mscFv/siPD-L1@LNP reconstructs the immune-excluded and immunosuppressive TME in the LLC tumor model. a Schematic illustration of the treatment and analysis schedule for mice bearing orthotopic LLC tumors. **b**–**f** Representative flow cytometric analysis profiles and relative quantifications of $CD8^+$ T cells ($CD45^+CD3^+CD8^+$) (**b**), Treg cells ($CD45^+CD4^+FOXP3^+$) (**c**), MDSCs ($CD45^+CD11b^+Gr\text{-}1^+$) (**d**), IFN-γ-secreting $CD8^+$ T cells ($CD45^+CD3^+CD8^+IFN\text{-}\gamma^+$) (**e**), and $CD8^+$ T cell proliferation ($CD45^+CD3^+CD8^+Ki67^+$) (**f**) within the TME following the indicated treatments. **g**–**i** Quantification of the infiltration of $CD45^+$ immune cells (**g**), $CD4^+$ T cells (**h**), and $CD8^+$ T cells (**i**) into lung tumors using flow cytometry. **j**–**n** ELISA analysis of IFN-γ (**j**), IL-2 (**k**), IL-12p70 (**l**), TNF-α (**m**), and IL-10 (**n**) levels in lung tumors of mice following the indicated treatments. Flow cytometry gating strategies are shown in Supplementary Fig. 28. All data are from $n = 5$ mice and are presented as mean ± s.d. Statistical analysis was performed using one-way ANOVA with Bonferroni's multiple comparisons test. *P* values as indicated. Source data are provided as a Source Data file.

https://doi.org/10.1038/s41467-025-63415-0

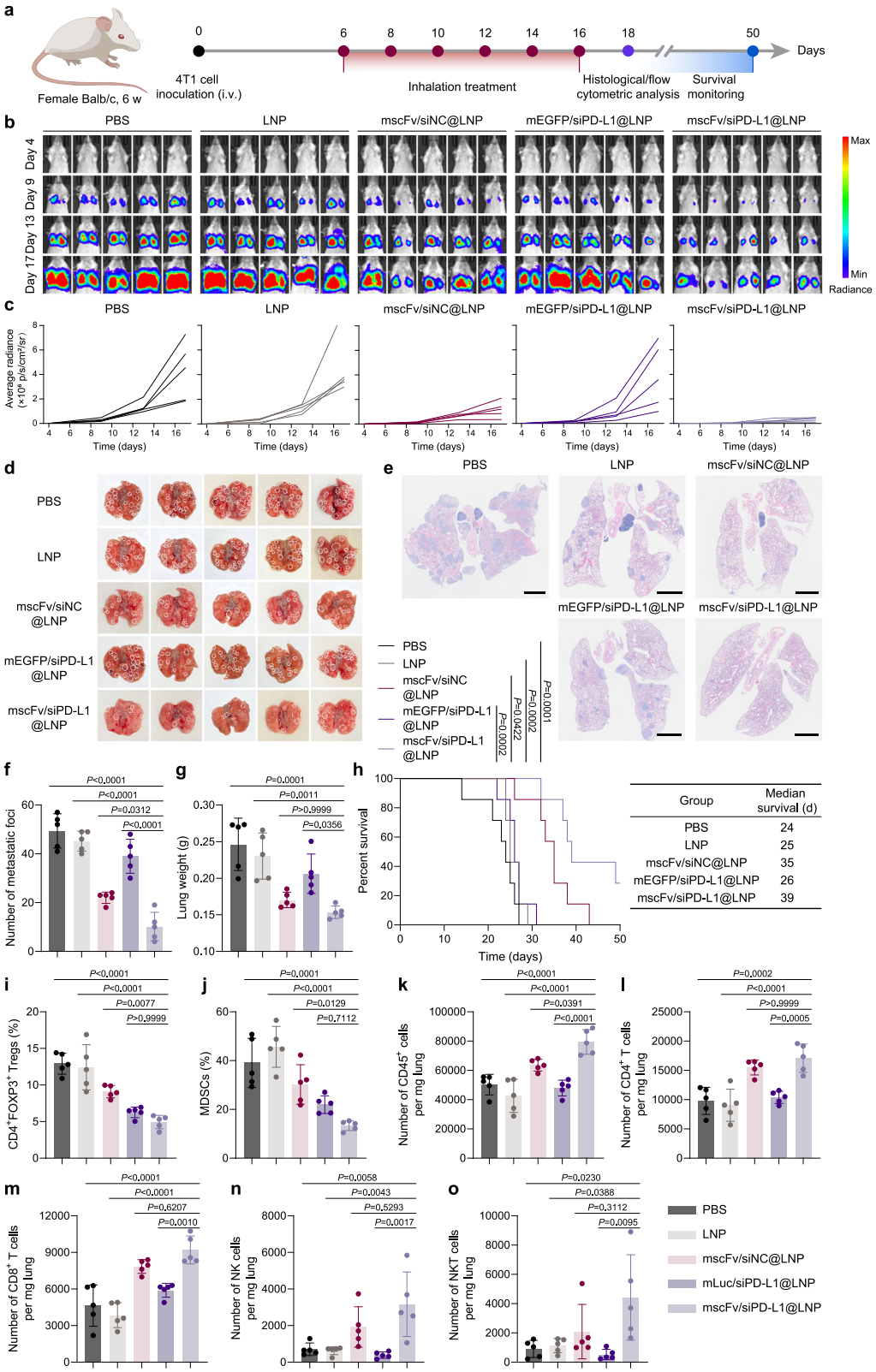

in the biomechanical properties of the tumor tissue, specifically a significant reduction in tumor stiffness. The disruption of collagen alignment and the decrease in tumor stiffness culminated in the enhanced infiltration of immune effector cells, a direct outcome of mscFv treatment. Thus, we have developed a strategy to increase the presence of immune cells around tumor cells by regulating the physical characteristics of the TME with mRNA-mediated antibody therapy. We suppose that cancer immunotherapies struggling with insufficient immune infiltration, such as CAR T and ICB therapies, could benefit from the combined use of mscFv@LNP.

Clinically available immunotherapies for lung cancer typically involve systemically administered antibody drugs. However, systemic circulation can lead to antibody accumulation in non-target organs, potentially causing side effects or toxicity, while also limiting the

Fig. 7 | Inhalation of mscFv/siPD-L1@LNP inhibits the progression of 4T1 breast cancer lung metastasis through TME reconstruction. a Schematic illustration of the inoculation of breast cancer lung metastasis via intravenous injection of 4T1-Luc cells and the following treatment and analysis schedules. **b**,**c** In vivo bioluminescence images reveal the tumor burden in mice receiving different treatments at indicated time points (**b**) and quantification of luciferase signals from each individual mouse (**c**) ($n = 5$ mice). **d** Representative image of metastatic lungs, with white circles indicating the metastatic foci. **e** Representative H&E-stained lung sections from mice following indicated treatments on day 18. Scale bar: 2 mm. Data were representative of three independent experimental replicates with similar results. **f** Number of metastatic foci on the lung surface following the indicated treatments ($n = 5$ mice). **g** Lung weight of mice from different treatment groups ($n = 5$ mice). **h** Kaplan–Meier survival curves and median survival time of tumor-bearing mice ($n = 7$ mice). **i**,**j** Quantified flow cytometry analysis of Treg cells ($CD45^+CD4^+FOXP3^+$) (**i**) and MDSCs ($CD45^+CD11b^+Gr\text{-}1^+$) (**j**) within the TME following the indicated treatments ($n = 5$ mice). **k**–**o** Quantification of the infiltration of $CD45^+$ immune cells (**k**), $CD4^+$ T cells (**l**), $CD8^+$ T cells (**m**), NK cells (**n**), and NKT cells (**o**) into lung tumors using flow cytometry ($n = 5$ mice). Flow cytometry gating strategies are shown in Supplementary Fig. 29. Results are presented as mean ± s.d. Statistical analysis was performed using one-way ANOVA with Bonferroni's multiple comparisons test (**f**,**g**, **i**–**o**) or by log-rank (Mantel–Cox) test (**h**). *P* values as indicated. Source data are provided as a Source Data file.

accessibility of antibodies to the lungs[45]. Additionally, the complex physiological environment poses challenges to antibody stability following intravenous injection. In contrast, inhalation allows for targeted enrichment of therapeutics in the lungs while minimizing systemic exposure, offering a promising alternative for pulmonary delivery in the treatment of lung diseases. Emerging pipelines are currently conducting clinical trials for various pulmonary diseases using inhaled mRNA-LNP therapies, underscoring the significant potential of this approach for clinical translation. In this study, an inhalable LNP was utilized, demonstrating excellent tolerance to the nebulizing process, with no changes in size, PDI, encapsulation efficiency, morphology, or its ability to mediate gene expression and silencing in vitro before and after nebulization. After inhalation, the LNP was exclusively distributed in the lungs, where it was efficiently internalized by cancer cells, leading to the effective expression of anti-DDR1 scFv. This inhaled LNP represents a non-invasive, effective, and safe method for localized delivery of multiple RNA payloads to the lung TME, with considerable translational potential. By transitioning the administration to an inhalation route based on inhaled LNP, it may also enhance the therapeutic outcomes of approved therapies for pulmonary diseases.

By leveraging localized delivery of mscFv and siPD-L1 with the advanced inhaled LNP platform, this approach is expected to effectively hinder lung tumor progression by targeting multiple facets of the hostile TME. In a mouse model of orthotopic lung cancer, the inhalation of mscFv/siPD-L1@LNP led to anti-DDR1 scFv expression and downregulation of PD-L1 levels in the tumor tissue. This treatment significantly slowed tumor growth and extended median survival, with half of the animals still alive 60 days after tumor inoculation, making it the only group with survivors. The antitumor response triggered by mscFv/siPD-L1@LNP was marked by a reduction in immunosuppressive cells and an increase in T cell infiltration. To expand the potential applications of this therapy, we explored its effects in a mouse model of 4T1 breast cancer lung metastasis, which also demonstrated promising results in controlling tumor progression. Inhalation of mscFv/siPD-L1@LNP showed pleiotropic therapeutic benefits in both orthotopic and metastatic lung cancers. This broad applicability is likely due to the widespread occurrence of immune exclusion and immunosuppression in various cancers, suggesting that mscFv/siPD-L1@LNP could be widely beneficial across multiple cancer types when paired with an appropriate administration route.

Although this study presents promising results, it has certain limitations. Combining mscFv/siPD-L1@LNP with therapies that recruit tumor-infiltrating immune cells, such as mRNA-based cytokines, could potentially elicit more robust antitumor responses. The inhalation of LNP resulted in broad internalization by various lung cell subtypes, rather than being exclusive to cancer cells. This led to the expression of anti-DDR1 scFv and the knockdown of PD-L1 in a wide range of cells. However, the broad expression profile of anti-DDR1 scFv is theoretically feasible, as it is secreted and functions extracellularly. While the downregulation of PD-L1 in non-targeted cells may occur, PD-L1 expression in various cell types, such as endothelial and dendritic cells, has also been shown to reduce antitumor immunity[46,47]. Despite these findings, developing a more specific inhaled LNP delivery system that targets lung cancer cells could broaden the applicability of this lung cancer therapy. Additionally, further studies are needed to optimize the dosing strategy for clinical application, potentially by leveraging self-amplifying or circular mRNA to achieve more sustained and elevated protein expression after administration. Permanent gene downregulation via mRNA-mediated CRISPR technology may enable a one-dose inhalation treatment for pulmonary diseases. Given that lung cancer frequently metastasizes in clinical settings, appropriate animal models of lung cancer metastasis should be established to evaluate the therapeutic effects of this inhalation therapy on both primary tumors and metastatic foci. While suppressing locoregional progression has been reported to delay metastatic spread[48], integrating this strategy with clinically approved systemic therapies or developing tumor-targeting LNP may further enhance metastasis inhibition. Future research may also prioritize repeating animal studies to ensure optimal reproducibility and assessing therapeutic efficacy in large animal models to facilitate clinical translation.

In conclusion, we developed a unique inhaled LNP approach that reconstructs the immune-excluded and immunosuppressive TME by combining mRNA-mediated antibody therapy and RNAi-based ICB therapy, effectively enhancing antitumor immunity for lung cancer treatment. By disrupting collagen fiber alignment with mRNA encoding anti-DDR1 scFv, the infiltration of immune effector cells was significantly improved. Simultaneously, siRNA-mediated PD-L1 knockdown alleviated immunosuppression in the TME, restoring the cancer-killing ability of infiltrating immune cells. This inhalation therapy contributed to the inhibition of tumor progression in both orthotopic and metastatic mouse models of lung cancer. Given the widespread presence of a hostile TME characterized by insufficient immune infiltration and immunosuppression in various cancers, this strategy could be applied to a broad range of tumor types and enhance the efficacy of other cancer immunotherapies.

Methods

Materials

1,2-Dioctadecanoyl-*sn*-glycero-3-phosphocholine (DSPC), 1,2-dimyristoyl-rac-glycero-3-methoxypolyethylene glycol-2000 (DMG-PEG2000), and cholesterol were purchased from AVT (Shanghai) Pharmaceutical Tech Co., Ltd. siPD-L1 and siNC were synthesized by Suzhou Biosyntech Co., Ltd. Antibodies used for flow cytometry, western blot, ELISA, and immunofluorescence staining are listed in Supplementary Data 1. ELISA kits were obtained from Neobioscience Technology Co., Ltd. Primers for RT-qPCR were synthesized by Suzhou Genewiz Biotechnology Co. Ltd., with sequences provided in Supplementary Table 1.

Cell culture

LLC-Luc, B16F10, 4T1-Luc, A549, H1975, H460, HEK293T, RAW 264.7, and BEAS-2B cell lines were obtained from ATCC. LLC-Luc, A549, HEK293T, RAW 264.7, and BEAS-2B cells were cultured in DMEM (Gibco) supplemented with 10% fetal bovine serum (FBS, Gibco) and 1% penicillin/streptomycin (Gibco). B16F10, 4T1-Luc, H1975, and H460 cells were cultured in RPMI 1640 (Gibco) supplemented with 10% FBS

and 1% penicillin/streptomycin. All cells were maintained at 37 °C in a humidified atmosphere with 5% CO_2.

CD8 T cells were prepared from healthy C57BL/6 mice. Briefly, spleens were collected and processed into a single-cell suspension by grinding and filtering through a 70-μm nylon strainer. After red blood cell lysis, CD8 T cells were isolated using the MojoSort™ Mouse CD8 T Cell Isolation Kit (BioLegend) according to the manufacturer's instructions. The isolated CD8 T cells were resuspended in RPMI 1640 supplemented with 10% FBS, 1% penicillin/streptomycin, and 0.1% 2-mercaptoethanol (Thermo Fisher Scientific) and then cultured in a 48-well plate pretreated with anti-mouse CD3 and CD28 antibodies (Bio X Cell). The cells were ready for use after 48 h of activation.

Experimental animal models

Female C57BL/6 mice (aged 6–8 weeks), female BALB/c mice (aged 6 weeks), and male C57BL/6 mice (aged 6–8 weeks) were purchased from Shanghai Lingchang Biotechnology Co., Ltd. and housed in a specific pathogen-free-grade animal facility. The mice were maintained under a 12-h dark/light cycle, with an ambient temperature of 20–22 °C and air humidity of 40–70%. All animal experiments were conducted following protocols approved by the Institutional Animal Care and Use Committee of Shanghai Jiao Tong University.

For the orthotopic LLC tumor model, C57BL/6 mice were anesthetized, and the surgical area was shaved and sterilized. A 5 mm incision was made below the left scapula to expose the costal layer. A total of 2×10^5 LLC-Luc cells in 50 μL of PBS containing 20% Matrigel (Corning) were injected through the chest wall into the left lung lobe using an insulin syringe with a 29 G needle. The incision was then closed using a skin clip. This procedure achieved a tumor implantation success rate of over 95% with no surgery-related mortality. For the metastatic lung cancer model, 1×10^5 4T1-Luc cells in 200 μL of PBS were intravenously injected into BALB/c mice via the tail vein. In both lung cancer mouse models, mice were euthanized when body weight loss exceeded 20%, and the maximal body weight loss permitted by the guidelines was not exceeded in any animal.

Synthesis of mRNA

Anti-DDR1 scFv mRNA (mscFv), firefly luciferase mRNA (mLuc), and EGFP mRNA (mEGFP) were synthesized through in vitro transcription (IVT). Briefly, the plasmids containing the open reading frame (ORF), 5′ untranslated region (UTR), 3′ UTR, and polyadenylated tail were linearized using BsaI (New England Biolabs). IVT was carried out at 37 °C for 3 h using T7 RNA polymerase (APExBIO), with uridine-5′-triphosphate (UTP) replaced by N^1-methylpseudo-UTP (APExBIO), and a Cap1 structure was introduced using Cap1-GAG (Yeasen). The resulting mRNA was purified using the RNA Clean & Concentrator kit (Zymo Research), and its concentration was determined with a NanoDrop spectrophotometer (Thermo Fisher Scientific). All mRNAs were stored at −80 °C and thawed on ice before use.

Preparation, nebulization, and characterization of LNP

LNPs were formulated by mixing an aqueous phase containing RNA with an organic phase containing lipids. The ethanol phase was prepared by dissolving AA3-Dlin ionizable lipid, DSPC, cholesterol, and DMG-PEG2000 at a molar ratio of 60:20:19:1. The aqueous phase, containing mRNA, siRNA, or their combination, was formulated in 50 mM citrate buffer at pH 4.0. The weight ratio of ionizable lipid to RNA was fixed at 15:1. The aqueous and ethanol phases were rapidly mixed at a volume ratio of 3:1 and a total flow rate of 80 mL/min using a microfluidic device (Aitesen). The resulting LNPs were dialyzed against 50 mM Tris buffer at pH 7.0 for 5 h in a 3.5K MWCO dialysis cassette (Thermo Fisher Scientific).

For the nebulization of LNPs, 8 mg/mL poloxamer 188 in 25 mM HEPES buffer (pH 6.0) was used to dilute the LNPs to a final RNA concentration of 0.1 μg/μL. The solution was then added dropwise to an Aerogen Solo vibrating mesh nebulizer to generate the LNP aerosol.

The size distribution, hydrodynamic diameter, polydispersity index, and zeta potential of the LNPs were measured with a Malvern ZetaSizer Nano ZSE. The morphology of the LNPs was examined by transmission electron microscopy (Thermo Fisher Scientific). Encapsulation efficiency was determined using a Quant-iT™ RiboGreen RNA Assay Kit (Invitrogen) according to the manufacturer's instructions.

qPCR analysis

Total RNA from cells was extracted using TRIzol Reagent (Invitrogen). The RNA was reverse-transcribed into cDNA using HiScript IV RT SuperMix for qPCR (Vazyme). qPCR reactions were then performed with ChamQ SYBR qPCR Master Mix (Vazyme) on a CFX Opus 96 Real-Time PCR System (Bio-Rad). The relative expression levels of target genes were normalized to the GAPDH endogenous control and calculated using the $-2^{\Delta\Delta Ct}$ method.

Cellular uptake, gene transfection, and gene silencing efficiency of LNP and nebulized LNP

For the cellular uptake assay, LLC, B16F10, and 4T1 cells were cultured to 80% confluence, and FBS-free culture medium was added. The cells were incubated with Cy5-labeled mscFv/siPD-L1@LNP or nebulized mscFv/siPD-L1@LNP for 4 h. After digestion and washing, the proportion of Cy5-positive cells and the intensity of Cy5 were determined by flow cytometry.

LLC, B16F10, 4T1, A549, H1975, and H460 cells were seeded in a 24-well plate and cultured overnight. The cell culture medium was then replaced with an FBS-free medium, and the cells were treated with different LNP formulations. After 4 h of incubation, FBS was added to the plate to a final concentration of 10%. For evaluating gene transfection efficiency, the cells were harvested 24 h post-transfection and analyzed for GFP-positive cells by flow cytometry. To assess gene silencing efficiency, the cells were harvested 48 h post-transfection, stained with PE-anti-PD-L1 antibody, and the efficiency of PD-L1 knockdown was analyzed by flow cytometry.

Endocytosis mechanism study

LLC, B16F10, and 4T1 cells were seeded in 24-well plates and cultured overnight. To inhibit specific endocytic pathways, cells were pretreated with 1 μg/mL filipin to block caveolae-mediated endocytosis, 10 μg/mL EIPA to block macropinocytosis, or 10 μg/mL chlorpromazine to block clathrin-mediated endocytosis. After 30 min, cells were transfected with mEGFP@LNP for 4 h and then cultured for an additional 20 h. Transfection efficiency following each inhibitor treatment was analyzed by flow cytometry.

Lysosomal escape assay

4T1 cells were seeded in glass-bottom dishes and cultured overnight. The cells were then incubated with Cy5-labeled mscFv/siPD-L1@LNP. At predetermined time points, the LNP was removed, and cells were rinsed with PBS, followed by incubation with Lyso-Tracker Green (Beyotime) for 30 min at 37 °C. After three additional PBS washes, nuclei were stained with Hoechst 33342 (Beyotime) for 10 min at 37 °C. Fluorescence signals were acquired using a Leica STELLARIS 5 laser confocal microscope.

Western blot analysis

Cells were lysed with RIPA buffer (Beyotime) supplemented with 1% protease inhibitor mixture (Solarbio). The cell culture supernatant was centrifuged to remove cell debris. Protein concentration was measured using the bicinchoninic acid (BCA) assay (Vazyme). Samples were mixed with 5× protein loading buffer (Yeasen) and heated at 100 °C for 5 min. The denatured samples were separated by SDS-polyacrylamide gel electrophoresis and transferred to a polyvinylidene

difluoride (PVDF) membrane (Millipore) for immunoblotting. Non-specific binding was blocked with 5% non-fat milk. The membrane was incubated with primary antibodies overnight at 4 °C with gentle shaking, washed with PBST, and then incubated with secondary antibodies. Proteins were detected using Omni-ECL enhanced chemiluminescence (Epizyme) on a ChemiDoc Imaging System (Bio-Rad). The primary and secondary antibodies used and their dilutions are listed in Supplementary Data 1. Uncropped and unprocessed scans of all blots have been provided in the Source Data file.

IVIS spectrum imaging

C57BL/6 mice were administered mLuc@LNP via inhalation at a dose of 5 μg of mLuc per mouse. Six hours post-inhalation, the mice were intraperitoneally injected with 200 μL of D-Luciferin potassium salt (Yeasen, 15 mg/mL) and sacrificed 5 min later. Bioluminescent signals from the heart, liver, spleen, lung, and kidney were recorded using an in vivo imaging system (PerkinElmer).

Expression and purification of DDR1 scFv

HEK293T cells were cultured to 80% confluence and transfected with mscFv using Lipofectamine 3000 (Invitrogen). Three days post-transfection, the cell culture supernatant was harvested, centrifuged to remove cell debris, and concentrated using Amicon Ultra-15-10K centrifugal filters (Millipore). The resulting crude product was incubated with Ni-NTA His-Tag Purification Agarose (MedChemExpress) at 4 °C overnight, followed by gradient elution with imidazole at different concentrations. The purity of DDR1 scFv was confirmed by Coomassie blue staining and Western blot analysis. The concentration of DDR1 scFv was determined using the BCA assay.

Enzyme-linked immunosorbent assay

The expression of Flag-tagged DDR1 scFv protein in the lung and bronchoalveolar lavage fluid (BALF) was measured at different time points after a single-dose inhalation of mscFv@LNP containing 20 μg of mscFv. Briefly, the harvested lung tissue was lysed with RIPA lysis buffer containing protease inhibitor. The lysates were centrifuged, and the supernatant was collected. BALF was collected according to a previously reported method[27]. Briefly, after anesthesia and sacrifice, the mouse trachea was surgically exposed and cannulated with a small tube. Cold PBS was gently instilled into the lungs through the trachea and then carefully withdrawn. This lavage process was repeated several times, with the recovered fluid pooled on ice and subsequently centrifuged to collect the BALF. Protein concentration in the lung lysate and BALF was determined using the BCA assay.

For enzyme-linked immunosorbent assay (ELISA), 96-well microplates (Greiner) were precoated with 100 ng of recombinant DDR1 ECD protein (Sino Biological) overnight at 4 °C. Non-specific binding was blocked with 5% BSA for 1 h at 37 °C. Then, 100 μL of samples were added to the wells and incubated at 37 °C for 2 h. After washing three times with PBST, 100 μL of diluted DYKDDDDK tag monoclonal antibody was added. The plate was incubated for 1 h at 37 °C, then washed three times with PBST, and incubated with horseradish peroxidase (HRP)-conjugated anti-mouse IgG at 37 °C for 1 h. Following three additional washes with PBST, 100 μL of TMB substrate solution (APExBIO) was added and incubated for 20 min at room temperature. The reaction was stopped by adding stop solution (Beyotime), and the absorbance at 450 nm was measured using a microplate reader (Tecan).

Isolation of primary mouse lung fibroblasts (MLF)

MLF were isolated from 6- to 8-week-old C57BL/6 mice. Briefly, mice were euthanized, surface-sterilized, and dissected to expose the thoracic cavity. After cardiac perfusion with cold PBS, lungs were excised, rinsed with cold PBS, and minced into 1–2 mm^3 fragments. The tissue fragments were digested with 1 mg/mL collagenase type I (Yeasen) at 37 °C for 90 min. The enzymatic reaction was then neutralized with complete medium, and the mixture was centrifuged at 582×*g* for 3 min. Following removal of the supernatant, the cell pellet was washed twice, resuspended in complete DMEM, and cultured at 37 °C in a 5% CO_2 incubator. MLF gradually migrated out from the tissue fragments during the initial culture period. Cells at passages three to five were used for subsequent experiments.

Cell viability assay

BEAS-2B cells and primary MLF were seeded in a 96-well plate at a density of 5×10^3 cells per well and cultured overnight. The cells were then treated with mscFv@LNP at varying mRNA concentrations. 24 h after transfection, the culture medium was replaced with serum-free medium containing CCK-8 reagent (Beyotime), and cells were incubated for an additional hour at 37 °C. Absorbance at 450 nm was measured using a microplate reader (Tecan).

Co-culture assay

LLC, B16F10, and 4T1 cells were cultured overnight in a 24-well plate and then treated with different formulations at a total RNA dose of 1 μg per well. Four hours later, the LNP-containing culture medium was removed, and activated CD8 T cells were added to the wells at an effector-to-target ratio of 1:2. Following a 24-h incubation, both the cells in the supernatant and the attached cells were harvested. The cells were then stained with Annexin V-FITC, PI, anti-CD3 antibody, anti-granzyme B antibody, anti-IFN-γ antibody, and anti-TNF-α antibody, and analyzed by flow cytometry. The cytokine levels in the cell culture medium were analyzed by Western blot.

Pulmonary function test

Mice were anesthetized and tracheostomized for the insertion of a 14-gauge cannula connected to the FlexiVent system (SCIREQ). The ventilator delivered predefined oscillatory waveforms to measure respiratory parameters. Baseline respiratory mechanics were measured using the Snapshot protocol. The Quick Prime-3 protocol was applied to standardize lung volume history and quantify static compliance. A Deep Inflation maneuver was performed to recruit alveoli and evaluate lung hysteresis. Pressure-Volume (P-V) loops were generated through slow inflation and deflation to assess static compliance and elasticity. Data were analyzed using FlexiVent software, normalized for body weight and baseline physiology. System calibration was ensured, and anesthesia depth and body temperature were maintained throughout the procedure.

Second harmonic generation (SHG)

Tumor tissues were harvested, snap-frozen in liquid nitrogen, embedded in optimal cutting temperature (OCT) compound, and sectioned into 20-μm slices using a cryostat before being mounted onto slides. The frozen sections were thawed at room temperature and stained with propidium iodide to label the nuclei. SHG and fluorescence images were captured using an Olympus FVMPE-RS multiphoton excitation microscope. Collagen fibers were analyzed using CT-FIRE (V3.0 beta) and CurveAlign (V5.0 beta). For data acquisition, each group included five individual animals, with the data for each animal representing the average of three representative tissue sections.

Atomic force microscopy measurements

Tumor tissues were freshly harvested and embedded in OCT compound, then chilled to −20 °C for 30 min, followed by −80 °C for 2 h in an isopropanol environment. The tissue blocks were then sectioned into 20-μm-thick slices using a cryostat and mounted onto slides. The sections were immersed in PBS, and the Young's modulus of the tumor tissue was measured using the NanoWizard V BioAFM (Bruker).

Efficacy studies on in vivo orthotopic and metastatic lung cancer models

The successful establishment of mouse lung cancer models was confirmed 4 days post-inoculation using IVIS imaging. Mice were then randomly assigned to different treatment groups. Inhalation treatment began on day six post-inoculation and was administered every 2 days[49,50] for a total of six treatments. Each mouse received a total RNA dose of 2 mg/kg per treatment, with equivalent weights of siRNA and mRNA. Tumor growth was monitored during the treatment period using IVIS imaging. Two days after the final treatment, the mice were euthanized, and their lungs were excised for morphological recording and weight measurement. The lungs were then fixed in 4% paraformaldehyde, and the number of metastatic foci was counted.

Histological analysis

The harvested tissues were fixed in 4% paraformaldehyde and embedded in paraffin after dehydration. The tissues were then sectioned into 5-μm-thick slices and mounted on microscope slides. Prior to staining, the sections were deparaffinized and rehydrated. H&E, TUNEL staining, and picrosirius red staining were performed using staining kits (Servicebio) according to the manufacturer's instructions. For immunofluorescence staining, the slides were immersed in antigen retrieval solution and heated in a microwave to unmask the epitopes. After blocking non-specific binding with 5% BSA, the sections were incubated with the primary antibody overnight at 4 °C, followed by incubation with a fluorescently conjugated secondary antibody. The antibodies used and their dilutions are provided in Supplementary Data 1. The nuclei were stained with DAPI solution. The stained sections were examined and imaged using an Olympus BX53 microscope or a Leica SP8 laser confocal microscope.

Flow cytometry assay

Tumor tissues and tumor-bearing lungs were harvested, cut into small fragments, and digested in RPMI 1640 medium containing 2 mg/mL collagenase type IV (Yeasen) and 1.2 mg/mL hyaluronidase (Maokangbio) at 37 °C for 1.5 h. The digested tissues were filtered through a 40-μm cell strainer to obtain a single-cell suspension. After lysing the red blood cells, the cells were stained with the Zombie Aqua™ Fixable Viability Kit (BioLegend) to assess their live/dead status, then blocked to prevent non-specific binding of Fc receptors. Surface staining with fluorescently-labeled antibodies was subsequently performed on ice. For cytokine production analysis, cells were treated with Cell Activation Cocktail (with Brefeldin A, BioLegend) prior to staining. Intracellular staining was performed after fixing and permeabilizing the cells using the Cyto-Fast™ Fix/Perm Buffer Set (BioLegend). For nuclear marker staining, cells were fixed and permeabilized using the FOXP3 Fix/Perm Buffer Set (BioLegend). Data acquisition was carried out using a BD LSRFortessa™ X-20 Cell Analyzer and analyzed with FlowJo v10 software. The gating strategy is illustrated in Supplementary Figs. 26–29. Details of the antibodies used and their dilutions can be found in Supplementary Data 1.

In vivo biosafety analysis

To evaluate potential in vivo toxicity, healthy C57BL/6 mice were administered the aforementioned treatment regimen. One day after the final treatment, the animals were sacrificed. Major organs, including the heart, liver, spleen, lungs, and kidneys, were collected for H&E staining. Blood and serum samples were collected for hematological and biochemical analysis.

Statistical analysis

All statistical analysis were performed using GraphPad Prism 8.0.2 software. Data were presented as mean ± s.d. Statistical significance between two value sets were determined using two-tailed unpaired Student's *t*-test. For multiple comparisons, one-way ANOVA with Bonferroni's multiple comparisons test was used. Kaplan–Meier survival curves were analyzed using the log-rank (Mantel–Cox) test. Exact *P* values were indicated in the figures. Statistical significance was set at $P < 0.05$.

Reporting summary

Further information on research design is available in the Nature Portfolio Reporting Summary linked to this article.

Data availability

All data supporting the findings of this study are available within the paper and its Supplementary Information. Source data are provided with this paper.

References

1. Waldman, A. D., Fritz, J. M. & Lenardo, M. J. A guide to cancer immunotherapy: from T cell basic science to clinical practice. *Nat. Rev. Immunol.* **20**, 651–668 (2020).
2. Meric-Bernstam, F., Larkin, J., Tabernero, J. & Bonini, C. Enhancing anti-tumour efficacy with immunotherapy combinations. *Lancet* **397**, 1010–1022 (2021).
3. Kelly, P. N. The Cancer Immunotherapy Revolution. *Science* **359**, 1344–1345 (2018).
4. Jin, M.-Z. & Jin, W.-L. The updated landscape of tumor microenvironment and drug repurposing. *Signal Transduct. Target. Ther.* **5**, 166 (2020).
5. Chen, X. et al. Non-invasive activation of intratumoural gene editing for improved adoptive T-cell therapy in solid tumours. *Nat. Nanotechnol.* **18**, 933 (2023).
6. Melssen, M. M., Sheybani, N. D., Leick, K. M. & Slingluff, C. L. Jr Barriers to immune cell infiltration in tumors. *J. Immunother. Cancer* **11**, e006401 (2023).
7. Zhang, D. et al. Enhancing CRISPR/Cas gene editing through modulating cellular mechanical properties for cancer therapy. *Nat. Nanotechnol.* **17**, 777 (2022).
8. Grout, J. A. et al. Spatial positioning and matrix programs of cancer-associated fibroblasts promote T-cell exclusion in human lung tumor. *Cancer Discov.* **12**, 2606–2625 (2022).
9. Su, H. & Karin, M. Multifaceted collagen-DDR1 signaling in cancer. *Trends Cell Biol.* **34**, 406–415 (2024).
10. Sun, X. et al. Tumour DDR1 promotes collagen fibre alignment to instigate immune exclusion. *Nature* **599**, 673 (2021).
11. Liu, J. et al. A highly selective humanized DDR1 mAb reverses immune exclusion by disrupting collagen fiber alignment in breast cancer. *J. Immunother. Cancer* **11**, e006720 (2023).
12. Fu, H.-L. et al. Discoidin domain receptors: unique receptor tyrosine kinases in collagen-mediated signaling. *J. Biol. Chem.* **288**, 7430–7437 (2013).
13. Hegde, P. S. & Chen, D. S. Top 10 challenges in cancer immunotherapy. *Immunity* **52**, 17–35 (2020).
14. de Visser, K. E. & Joyce, J. A. The evolving tumor microenvironment: from cancer initiation to metastatic outgrowth. *Cancer Cell* **41**, 374–403 (2023).
15. Morad, G., Helmink, B. A., Sharma, P. & Wargo, J. A. Hallmarks of response, resistance, and toxicity to immune checkpoint blockade. *Cell* **184**, 5309–5337 (2021).
16. Zappasodi, R., Merghoub, T. & Wolchok, J. D. Emerging concepts for immune checkpoint blockade-based combination therapies. *Cancer Cell* **33**, 581–598 (2018).
17. Patsoukis, N., Wang, Q., Strauss, L. & Boussiotis, V. A. Revisiting the PD-1 pathway. *Sci. Adv.* **6**, eabd2712 (2020).
18. Kuzmov, A. & Minko, T. Nanotechnology approaches for inhalation treatment of lung diseases. *J. Control. Release* **219**, 500–518 (2015).
19. Vargason, A. M., Anselmo, A. C. & Mitragotri, S. The evolution of commercial drug delivery technologies. *Nat. Biomed. Eng.* **5**, 951–967 (2021).

20. Hu, B. et al. Therapeutic siRNA: state of the art. *Signal Transduct. Target. Ther.* **5**, 101 (2020).
21. Loira-Pastoriza, C., Todoroff, J. & Vanbever, R. Delivery strategies for sustained drug release in the lungs. *Adv. Drug Deliv. Rev.* **75**, 81–91 (2014).
22. Borghardt, J. M., Kloft, C. & Sharma, A. Inhaled therapy in respiratory disease: the complex interplay of pulmonary kinetic processes. *Can. Respiratory J.* **2018**, 2732017 (2018).
23. Abdelaziz, H. M. et al. Inhalable particulate drug delivery systems for lung cancer therapy: nanoparticles, microparticles, nanocomposites and nanoaggregates. *J. Control. Release* **269**, 374–392 (2018).
24. Tang, Z. et al. Inhaled mRNA nanoparticles dual- targeting cancer cells and macrophages in the lung for effective transfection. *Proc. Natl Acad. Sci. USA* **120**, e2304966120 (2023).
25. Rotolo, L. et al. Species-agnostic polymeric formulations for inhalable messenger RNA delivery to the lung. *Nat. Mater.* **22**, 369 (2023).
26. Liu, M., Hu, S., Yan, N., Popowski, K. D. & Cheng, K. Inhalable extracellular vesicle delivery of IL-12 mRNA to treat lung cancer and promote systemic immunity. *Nat. Nanotechnol.* **19**, 565–575 (2024).
27. Bai, X. et al. Inhaled siRNA nanoparticles targeting IL11 inhibit lung fibrosis and improve pulmonary function post-bleomycin challenge. *Sci. Adv.* **8**, eabn7162 (2022).
28. Bai, X. et al. Optimized inhaled LNP formulation for enhanced treatment of idiopathic pulmonary fibrosis via mRNA-mediated antibody therapy. *Nat. Commun.* **15**, 6844 (2024).
29. Li, Z. et al. Enzyme-catalyzed one-step synthesis of ionizable cationic lipids for lipid nanoparticle-based mRNA COVID-19 vaccines. *Acs Nano* **16**, 18936–18950 (2022).
30. Moll, S. et al. DDR1 role in fibrosis and its pharmacological targeting. *Biochim. Biophys. Acta Mol. Cell Res.* **1866**, 118474 (2019).
31. Ongusaha, P. P. et al. p53 induction and activation of DDR1 kinase counteract p53-mediated apoptosis and influence p53 regulation through a positive feedback loop. *EMBO J.* **22**, 1289–1301 (2003).
32. Juin, A. et al. Discoidin domain receptor 1 controls linear invadosome formation via a Cdc42-Tuba pathway. *J. Cell Biol.* **207**, 517–533 (2014).
33. Yu, W. et al. PD-L1 promotes tumor growth and progression by activating WIP and β-catenin signaling pathways and predicts poor prognosis in lung cancer. *Cell Death Dis.* **11**, 506 (2020).
34. Taufalele, P. V., Vanderburgh, J. A., Munoz, A., Zanotelli, M. R. & Reinhart-King, C. A. Fiber alignment drives changes in architectural and mechanical features in collagen matrices. *PLoS ONE* **14**, e0216537 (2019).
35. Dammeijer, F. et al. The PD-1/PD-L1-checkpoint restrains T cell immunity in tumor-draining lymph nodes. *Cancer Cell* **38**, 685 (2020).
36. Li, F. et al. mRNA lipid nanoparticle-mediated pyroptosis sensitizes immunologically cold tumors to checkpoint immunotherapy. *Nat. Commun.* **14**, 4223 (2023).
37. Rudqvist, N.-P. et al. Immunotherapy targeting different immune compartments in combination with radiation therapy induces regression of resistant tumors. *Nat. Commun.* **14**, 5146 (2023).
38. Kuczek, D. E. et al. Collagen density regulates the activity of tumor-infiltrating T cells. *J. Immunother. Cancer* **7**, 68 (2019).
39. Zou, W. P. Immunosuppressive networks in the tumour environment and their therapeutic relevance. *Nat. Rev. Cancer* **5**, 263–274 (2005).
40. Rafiq, S., Hackett, C. S. & Brentjens, R. J. Engineering strategies to overcome the current roadblocks in CAR T cell therapy. *Nat. Rev. Clin. Oncol.* **17**, 147–167 (2020).
41. Chen, D. S. & Mellman, I. Oncology meets immunology: the cancer-immunity cycle. *Immunity* **39**, 1–10 (2013).
42. Patel, S. A. & Minn, A. J. Combination cancer therapy with immune checkpoint blockade: mechanisms and strategies. *Immunity* **48**, 417–433 (2018).
43. Sen, S. et al. A phase I first-in-human study of PRTH-101, an IgG1 monoclonal antibody targeting DDR1, as a monotherapy and combined with pembrolizumab in patients with advanced solid malignancies. *Ann. Oncol.* **34**, S649–S650 (2023).
44. Jin, S. et al. Emerging new therapeutic antibody derivatives for cancer treatment. *Signal Transduct. Target. Ther.* **7**, 39 (2022).
45. Melero, I., Castanon, E., Alvarez, M., Champiat, S. & Marabelle, A. Intratumoural administration and tumour tissue targeting of cancer immunotherapies. *Nat. Rev. Clin. Oncol.* **18**, 558–576 (2021).
46. Cousin, N. et al. Lymphatic PD-L1 expression restricts tumor-specific CD8+ T-cell responses. *Cancer Res.* **81**, 4133–4144 (2021).
47. Peng, Q. et al. PD-L1 on dendritic cells attenuates T cell activation and regulates response to immune checkpoint blockade. *Nat. Commun.* **11**, 4835 (2020).
48. Katipally, R. R., Pitroda, S. P., Juloori, A., Chmura, S. J. & Weichselbaum, R. R. The oligometastatic spectrum in the era of improved detection and modern systemic therapy. *Nat. Rev. Clin. Oncol.* **19**, 585–599 (2022).
49. Mao, C. et al. In situ editing of tumour cell membranes induces aggregation and capture of PD-L1 membrane proteins for enhanced cancer immunotherapy. *Nat. Commun.* **15**, 9723 (2024).
50. Li, Z. et al. Targeting pulmonary tumor microenvironment with CXCR4-inhibiting nanocomplex to enhance anti-PD-L1 immunotherapy. *Sci. Adv.* **6**, eaaz9240 (2020).

Acknowledgements

The work was funded by the National Key Research and Development Program of China (2023YFC2606003), the Natural Science Foundation of Shanghai (23ZR1427600), "Open Competition to Select the Best Candidates" Key Technology Program for Nucleic Acid Drugs of NCTIB (Grant No. NCTIB2022HS02002), and 2025 Key Technology Research Program in Cell and Gene Therapy (25J22800300). X.X. acknowledges support from the National Science Foundation (2001606) and the Gustavus and Louise Pfeiffer Research Foundation Award.

Author contributions

B.H., X.X., and X.-Q.Z. conceived the study and designed the experiments. B.H. performed most experiments and wrote the original manuscript. Q.C. contributed to the design of LNP. C.Z. assisted with sample preparation for the animal flow cytometry study. B.H., W.S., Z.L., X.X., and X.-Q.Z. analyzed and discussed the results. X.X. and X.-Q.Z. supervised the research and reviewed and edited the manuscript.

Competing interests

The authors declare no competing interests.

Additional information

Supplementary information The online version contains supplementary material available at https://doi.org/10.1038/s41467-025-63415-0.

Correspondence and requests for materials should be addressed to Xiaoyang Xu or Xue-Qing Zhang.

Peer review information *Nature Communications* thanks Ke Cheng, Kaisa Lehti and the other anonymous reviewer(s) for their contribution to the peer review of this work. A peer review file is available.

Reprints and permissions information is available at http://www.nature.com/reprints

Publisher's note Springer Nature remains neutral with regard to jurisdictional claims in published maps and institutional affiliations.

Open Access This article is licensed under a Creative Commons Attribution-NonCommercial-NoDerivatives 4.0 International License, which permits any non-commercial use, sharing, distribution and reproduction in any medium or format, as long as you give appropriate credit to the original author(s) and the source, provide a link to the Creative Commons licence, and indicate if you modified the licensed material. You do not have permission under this licence to share adapted material derived from this article or parts of it. The images or other third party material in this article are included in the article's Creative Commons licence, unless indicated otherwise in a credit line to the material. If material is not included in the article's Creative Commons licence and your intended use is not permitted by statutory regulation or exceeds the permitted use, you will need to obtain permission directly from the copyright holder. To view a copy of this licence, visit http://creativecommons.org/licenses/by-nc-nd/4.0/.

© The Author(s) 2025